nature nanotechnology

ARTICLES

https://doi.org/10.1038/s41565-021-01040-w

Three-dimensional transistor arrays for intra- and inter-cellular recording

Yue Gu[1,2], Chunfeng Wang[2], Namheon Kim[2], Jingxin Zhang[1], Tsui Min Wang[3], Jennifer Stowe[3], Rohollah Nasiri[4], Jinfeng Li[5], Daibo Zhang[3], Albert Yang[3], Leo Huan-Hsuan Hsu[6], Xiaochuan Dai[6], Jing Mu[2], Zheyuan Liu[7], Muyang Lin[2], Weixin Li[2], Chonghe Wang[2], Hua Gong[2], Yimu Chen[2], Yusheng Lei[2], Hongjie Hu[1,2], Yang Li[2], Lin Zhang[2], Zhenlong Huang[2], Xingcai Zhang[8], Samad Ahadian[4], Pooja Banik[2], Liangfang Zhang[2], Xiaocheng Jiang[6], Peter J. Burke[9], Ali Khademhosseini[4], Andrew D. McCulloch[3] and Sheng Xu[1,2,3,10,11] ✉

Electrical impulse generation and its conduction within cells or cellular networks are the cornerstone of electrophysiology. However, the advancement of the field is limited by sensing accuracy and the scalability of current recording technologies. Here we describe a scalable platform that enables accurate recording of transmembrane potentials in electrogenic cells. The platform employs a three-dimensional high-performance field-effect transistor array for minimally invasive cellular interfacing that produces faithful recordings, as validated by the gold standard patch clamp. Leveraging the high spatial and temporal resolutions of the field-effect transistors, we measured the intracellular signal conduction velocity of a cardiomyocyte to be 0.182 m s^{-1}, which is about five times the intercellular velocity. We also demonstrate intracellular recordings in cardiac muscle tissue constructs and reveal the signal conduction paths. This platform could provide new capabilities in probing the electrical behaviours of single cells and cellular networks, which carries broad implications for understanding cellular physiology, pathology and cell–cell interactions.

Electrophysiological approaches have been used to elucidate and modulate the activities of electrogenic cells[1,2]. Transmembrane potentials associated with ionic fluxes between the cytosol and interstitium underlie the macroscopic electrophysiological characteristics of tissues and organs[3]. Research in this field is largely driven by the use of well-established tools for high-fidelity transmembrane potential recording in single cells or multicellular networks. Ideally, the recording needs to be highly accurate and scalable over a large area. Sensor contact with the cytoplasm is needed for direct intracellular sensing[4,5]. Patch clamping, in its various forms[6], has been the gold standard for recording transmembrane potentials. However, it is challenging to perform on multiple cells simultaneously. Methods based on voltage-sensitive dyes can record multiple cells in parallel but are plagued by cytotoxicity and low temporal resolution[7]. Therefore, a variety of potentially scalable approaches have been explored for intracellular electrical recording, including passive electrodes and active field-effect transistors (FETs). Passive electrodes have difficulties in picking up subthreshold and low-amplitude cellular signals due to their intrinsically large impedance[8]. Active FETs, with minimal access impedance and wide bandwidths, have shown great promise for either intracellular sensing or scalability, but have not yet been demonstrated to meet the requirements for both[9].

Here we report a scalable three-dimensional (3D) FET array for sensing intracellular as well as intercellular signal conduction in both two-dimensional (2D) cultures and 3D tissue constructs. This array has enabled us to directly measure intracellular signal conduction velocity, which is closely related to organ pathology, where its irregularities may be implicative of severe diseases[10]. We demonstrate that the intracellular signal conduction velocity in cardiomyocytes is about five times the intercellular conduction velocity reported conventionally. The difference between intracellular and intercellular velocities indicates the coupling efficacy between cells. We also demonstrate intracellular recordings of cardiomyocytes in cardiac muscle tissue constructs, revealing the signal conduction paths, which paves the way for intracellular electrophysiological studies in vivo.

Fabrication and characterization of the 3D FET arrays

The 3D FET array was constructed using a compressive buckling technique[11] (Fig. 1a). First, a multilayered 2D precursor was fabricated by standard micro/nanofabrication techniques (Fig. 1b, left). The precursor was transferred and selected regions were bonded onto a prestrained elastomer substrate, after which the prestrain of the elastomer substrate was released. The compression caused the 2D precursor to buckle at predesigned hinge locations to form a 3D structure (Fig. 1b, right, and Supplementary Video 1). To verify the electrical functions of the device before and after the buckling, dummy structures consisting of Au and Si–Au were processed in

[1]Materials Science and Engineering Program, University of California San Diego, La Jolla, CA, USA. [2]Department of NanoEngineering, University of California San Diego, La Jolla, CA, USA. [3]Departments of Bioengineering and Medicine, University of California San Diego, La Jolla, CA, USA. [4]Terasaki Institute for Biomedical Innovation, Los Angeles, CA, USA. [5]Department of Physics and Astronomy, University of California Irvine, Irvine, CA, USA. [6]Department of Biomedical Engineering, Tufts University, Medford, MA, USA. [7]Electrochemical Energy Laboratory, Massachusetts Institute of Technology, Cambridge, MA, USA. [8]School of Engineering and Applied Sciences, Harvard University, Cambridge, MA, USA. [9]Department of Chemical Engineering and Materials Science, University of California Irvine, Irvine, CA, USA. [10]Department of Radiology, University of California San Diego, La Jolla, CA, USA. [11]Department of Electrical and Computer Engineering, University of California San Diego, La Jolla, CA, USA. ✉e-mail: shengxu@ucsd.edu

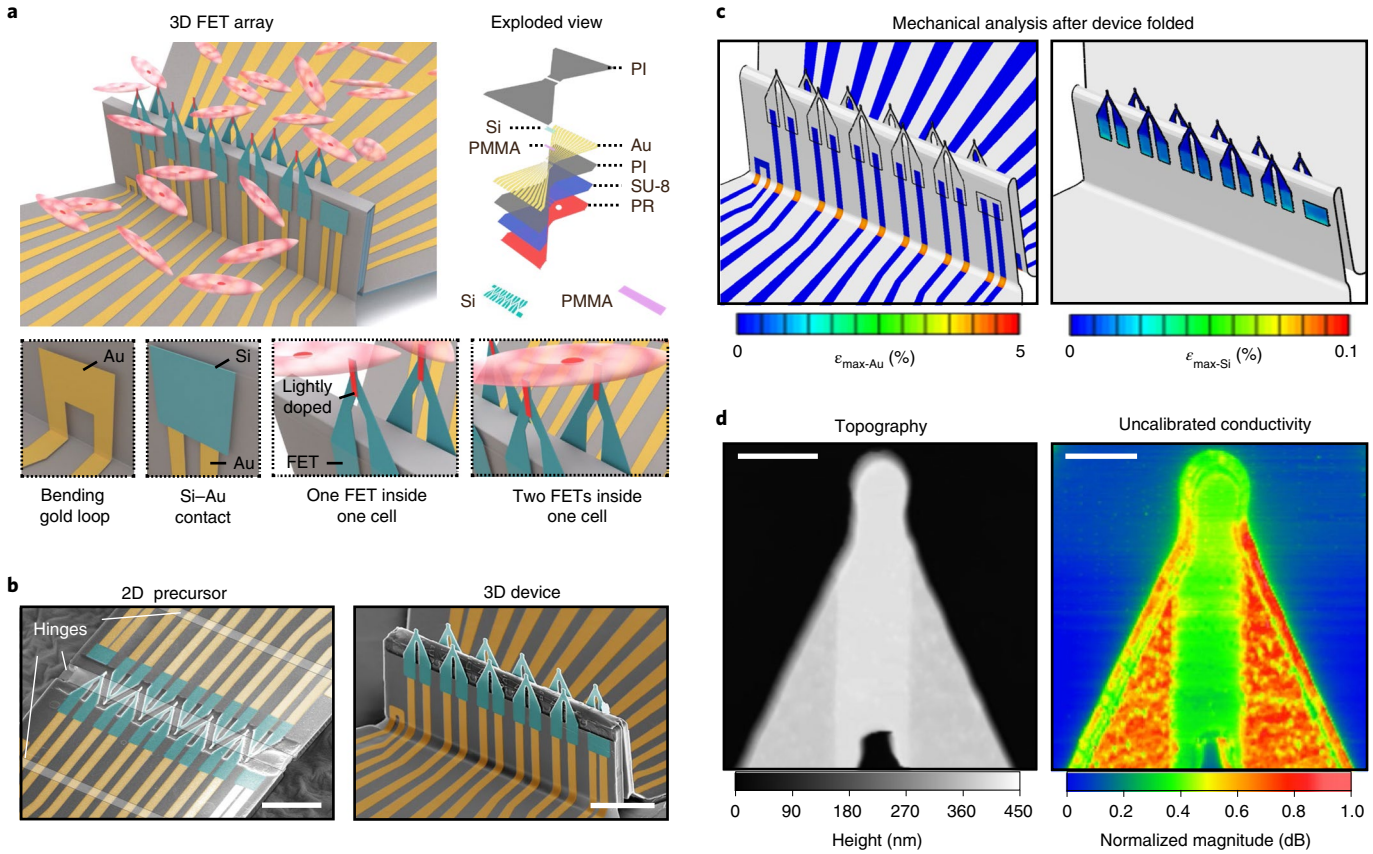

Fig. 1 | 3D FET arrays by compressive buckling. a, Schematic images showing a 10-FET array interfacing a group of cardiomyocytes. The exploded view illustrates the multilayered design of the FET array (top right). The images at the bottom show, from left to right, a Au loop for checking the electrical conductivity after the device buckles, a Au–Si bilayer for probing the quality of the electrical contact after the device has been soaked in an acidic solution, one FET recording intracellular signals and two FETs in the same cell to study intracellular signal conductions. The red area on each FET denotes the lightly doped channel. PI, polyimide; SU-8, an epoxy-based polymer; PR, photoresist. **b**, False-coloured SEM images showing the transformation from a 2D precursor (left) to a 3D 10-FET array (right). Each FET has a tapering tip (5 μm long and 1–2 μm wide). Scale bars, 50 μm. **c**, Finite element analysis of a 3D 10-FET array. The maximum strains (ε) in Au (left) and Si (right) are well below the fracture limit of each material. **d**, Images of a FET tip obtained by atomic force microscopy (left) and scanning microwave microscopy (right). The former operates in contact mode and maps the surface topography of the FET. The latter maps the uncalibrated conductivity, and thus the admittance distribution, of the FET. A lightly doped region can be clearly distinguished in both images. Because of the over-etching of the oxide doping mask, the lightly doped region is slightly thicker than the surrounding heavily doped regions (Supplementary Note 1). Also, the lightly doped region exhibits a lower conductivity than the surrounding heavily doped regions (Methods, Supplementary Note 2 and Extended Data Fig. 2). Scale bars, 2 μm.

parallel and used as checkpoints (Fig. 1a, bottom). The 3D structure was coated with a bilayer of Parylene C and SiO_2 for electrical insulation and hydrophilic surface functionalization. The compressive buckling technique enabled us to fabricate arrays at various scales with different materials, layouts, dimensions and geometries. For further details see Methods, Supplementary Note 1, Extended Data Fig. 1 and Supplementary Figs. 1–3.

The 3D geometry allows the FET to penetrate the cell membrane and record low-amplitude subthreshold signals inside the cell. The small sensor tip (1–2 μm) penetrates the cell membrane with minimal invasiveness[12]. The device layout was designed to allow interfacing with multiple cells and even to have two FETs in the same cell (Fig. 1a, bottom). To ensure that the entire device was mechanically robust, we carried out theoretical and experimental studies to optimize the materials and their dimensions, such as the use of low-molecular-weight poly(methyl methacrylate) (PMMA) and a thick acid-resistant photoresist as sacrificial layers. As simulated by finite element analysis (Fig. 1c), after the optimization, the maximum strains of the Au and Si in the buckled 3D device were 4 and 0.05%, respectively, which are below their failure strains[13,14]. The buckling process was reversible. Under an externally applied tensile strain, the 3D device unfolded and recovered the 2D geometry. The softness of the device reduces the mechanical mismatch between the cell culture and the device[15]. The FET's structure was verified by atomic force microscopy and scanning microwave microscopy in topographic and reflection coefficient mapping modes, respectively (Fig. 1d and Extended Data Fig. 2).

The ability of a FET to accurately capture cellular signals, especially low-amplitude subthreshold potentials, depends on its sensitivity and noise level. The sensitivity is determined by the transconductance, which is tunable by the doping profile of the conduction channel (Supplementary Note 3). Lower doping concentrations typically yield higher sensitivities[16]. However, noise level also increases with sensitivity, especially in the low-frequency regime[17]. Therefore, we used the sensitivity-to-noise ratio to characterize the FET performance. By tailoring the doping time, we could precisely control the sheet resistance and thus doping concentrations in different regions of the FET, leading to a selectively doped n^+nn^+ (n-type semiconductor with more heavily doped drain and source regions than the gate region) structure. The n^+nn^+

structure is crucial for high sensitivity and operational reliability at zero gate bias because it operates in the 'ON' state with zero gate bias, which avoids the irreversible Faradaic reactions induced by the high gate voltage during signal recording observed with other FET structures (Extended Data Fig. 3 and Supplementary Note 4). For the FET geometry shown in Fig. 1d, we optimized the doping time to achieve the highest sensitivity-to-noise ratio (Fig. 2a). The sensitivity-to-noise ratios of the selectively doped FETs were much higher than those of FETs with low uniform doping (that is, only background doping from the substrate) or high uniform doping (Fig. 2b and Extended Data Fig. 3).

We characterized the transport behaviour of a 10-FET array in a water-gate configuration (Methods and Supplementary Fig. 4). The output characteristics of a FET in the array showed typical n-channel properties under various gate biases (Fig. 2c(i)). Furthermore, each FET exhibited large conductance under various drain potentials at zero gate bias (Fig. 2c(ii)), which is crucial for sensing cellular electrophysiological signals (Supplementary Note 4). The 10 FETs showed an average conductance of $0.9 \pm 0.3\,\mu S$ (Fig. 2d(i)) and an average transconductance of $7.5 \pm 2.0\,\mu S\,V^{-1}$ (Fig. 2d(ii)). The transconductance is greater than, and its relative standard deviation (that is, its coefficient of variation) is comparable to, those of devices synthesized by bottom-up methods[18], which can be attributed to the high material quality of the device-grade Si and controllable fabrication process. The high performance allows the FETs to record low-amplitude subthreshold cellular signals[3].

After transforming from two to three dimensions, the 10 FETs showed a <0.2% variation in conductance and a <0.5% variation in transconductance (Fig. 2e), which validates the mechanical and electrical robustness of the 3D FETs. The 10 FETs exhibited comparable conductance before and after immersion in saline solution (Fig. 2f), showing neglectable changes in surface charge and minimal current leakage through the insulation layers. Moreover, the FETs exhibited consistently high sensitivities over a range of pH (from 6.7 to 7.6) and temperatures (from 21 to 50 °C), demonstrating their tolerance to chemical and thermal conditions in various cell culture media (Extended Data Fig. 4). The stability of the FETs is primarily attributed to the insulating gate dielectric materials. The type of gate dielectric materials will not affect the FETs' sensitivity (Extended Data Fig. 4).

To ensure that we could record dynamic and transient ionic signals, we characterized the temporal response of the FETs. Pulse signals with a rise and fall time of 5 ns to 50 ms were applied to the gate, and the channel signals of the FETs were recorded. The FETs showed a short intrinsic response time to the input gate signals (≤712 ns), which is shorter than previously reported values due to its optimized small gate dielectric thickness[19] (Supplementary Note 5 and Supplementary Fig. 5). Due to the limit of the sampling rate of the digitizer (100 kHz maximum), the entire recording system has a temporal resolution of 0.01 ms. The recorded channel signal shows a response time of 0.1 ms (Fig. 2g(i)), which is sufficient to accurately record common ionic activities (typically >1 ms)[20]. Note that there is a capacitance-induced overshoot on the rising and falling edges of the response. The capacitance arises from electrode–ionic solution coupling, which can be neglected in cellular measurements because of the localized coupling between the membrane potential and the FET (for more details see Supplementary Note 3)[21]. In repeated measurements, the start and saturation times of the FET's response remained unchanged, showing that it can accurately follow the rapid input signals (Fig. 2g(ii)). With different rising/falling times (0.1–50 ms) of the input signal, the conductance changes were within ~1.5%, which is typical for FETs (Fig. 2g(iii))[21]. Additionally, the FETs can faithfully record simulated cellular action potentials resembling those produced by pacemaker and non-pacemaker cardiomyocytes, with frequencies of 1–10 Hz, covering the typical firing frequencies of electrogenic cells. More discussions related to the response time of the FET are presented in Supplementary Notes 6–8 and Supplementary Fig. 6.

We coated a phospholipid bilayer onto the FETs to facilitate internalization into cells[4] and to enable good sealing at the FET–cell interface. Either small unilamellar vesicles of extracted red blood cell membranes or synthetic phospholipid bilayer materials (1,2-dimyristoyl-*sn*-glycero-3-phosphocholine) were used[4,22] (Methods). Fluorescent imaging confirmed the successful coating of the phospholipids on all FETs before and after buckling (Supplementary Note 9 and Supplementary Figs. 7 and 8). To illustrate the internalization process, when the FET is near the cell, it records the membrane potential extracellularly. The equivalent circuit model reveals an attenuated signal (V_c) due to the membrane impedance (which is composed of membrane resistance (R_m) and membrane capacitance (C_m) connected in parallel) and the shunt via the small spreading resistance (R_s). As the FET approaches the cell, the phospholipid coating spontaneously fuses with the cell membrane with minimal invasiveness to the cell, realizing intracellular sensing. The tight interfacial sealing maximizes the spreading resistance R_s (that is, minimizes leakage current) (Supplementary Fig. 8).

Recording intracellular action potentials

Full-amplitude signals contain quantitative information on ionic activities inside the cell[4,21]. The full amplitude depends on many factors, including the type, culture conditions and physiological status of the cell[4,21,23]. The FET arrays in this work can measure full-amplitude signals comparable to those acquired by the whole-cell patch clamp[21,24].

Cell viability test results proved that neither the construction materials nor the signal recording of the FET showed cytotoxicity towards HL-1 cardiac muscle cells (Supplementary Fig. 9). A Ca^{2+} sparks assay confirmed the electrophysiological activity of the HL-1 cells (Methods, Supplementary Figs. 10 and 11, and Supplementary Videos 2–4). Full-amplitude action potentials were stably recorded by both the FET and a whole-cell patch clamp (Fig. 3a and Supplementary Fig. 12). The amplitudes, morphologies and firing patterns of the acquired potentials by those two techniques show strong agreement, revealing the ideal coupling and faithful recording of the intracellular signals by the FETs. The minor discrepancies are within the standard fluctuations expected due to differences in cellular physiology and measurement set-ups[23,25] (Supplementary Note 10). Importantly, the FETs could record subthreshold signals due to their high sensitivity-to-noise ratios. Primary cells exhibit natural and primitive electrophysiological characteristics akin to their intrinsic states in live animals. The FET was able to record action potentials from spontaneously firing neonatal and adult mouse cardiomyocytes with results similar to those of the whole-cell patch[25–27] (Fig. 3b,c). The amplitude of each spike in the same recording fluctuates as a result of the contractile movements of the cells[24].

The phospholipid coating on the FETs plays a crucial role in the intracellular recording. Continuous intracellular signal recordings on HL-1 cells could be extended to over 70 s (Supplementary Fig. 13), the longest reported by an intracellular FET sensor. A phospholipid coating could last three cell insertions before refunctionalization was needed to achieve a stable intracellular recording (Supplementary Fig. 14). Without the phospholipid coating, the FET could still mechanically rupture the cellular membrane and access the cytoplasm sometimes. However, those recordings showed higher noise levels, lower signal amplitudes and fluctuating signal baselines due to the highly unstable FET–cell interface (Supplementary Fig. 15). Signals recorded without the phospholipid coating gradually transformed from intracellular to extracellular, probably because the ruptured cell membranes fused again and expelled the FET[24] (Supplementary Figs. 16–18).

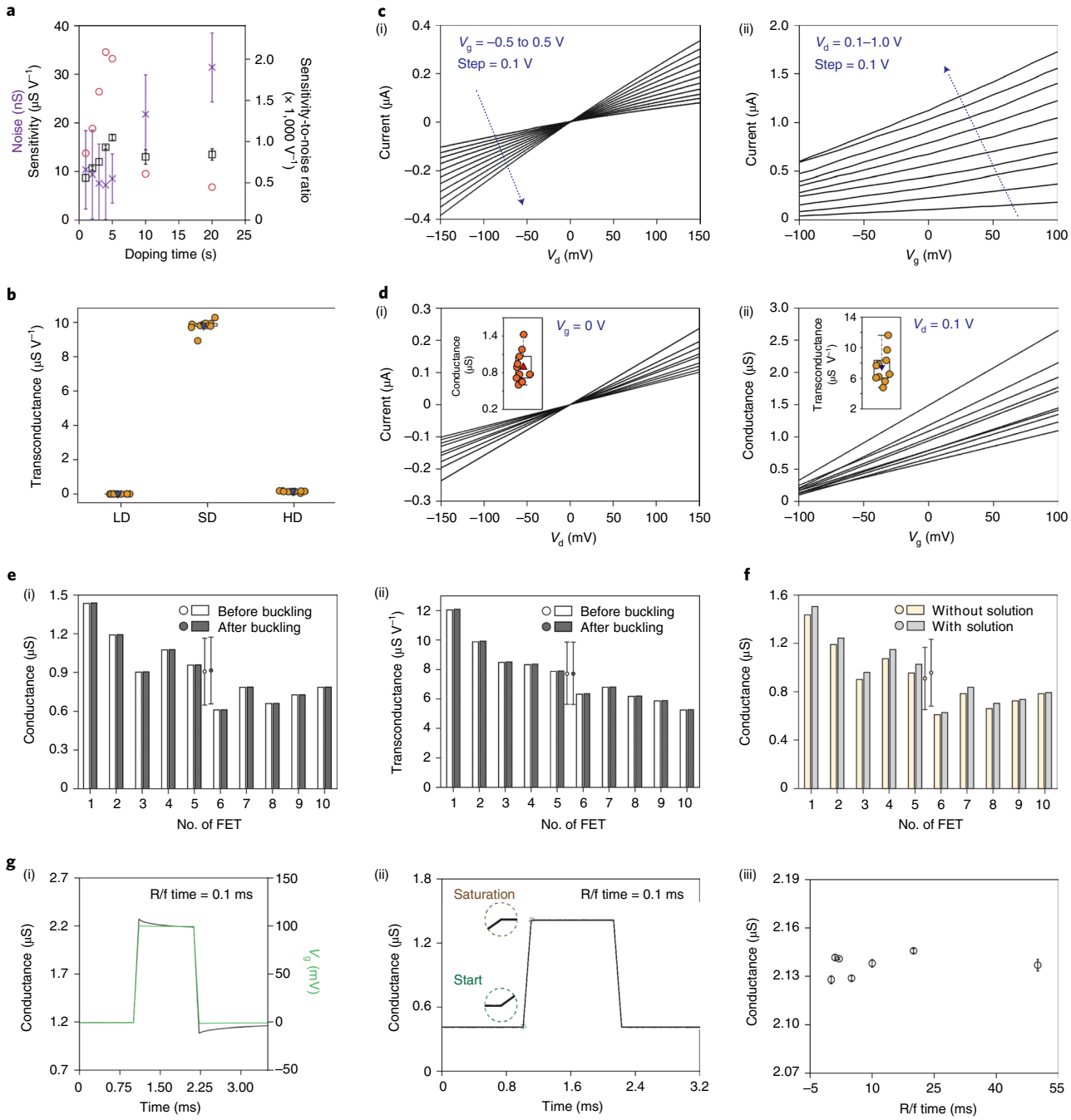

Fig. 2 | Electrical optimization and characterization of the FETs. a, The sensitivity-to-noise ratio of the FET as a function of doping time in the lightly doped region. A doping time of <4 s leads to a lower current in the conduction channel. A doping time of >4 s results in higher noise, because of a larger number of traps generated by doping-induced defects. Square, sensitivity; cross, noise; circle, sensitivity-to-noise ratio. **b**, Calculated transconductances of three devices with different doping profiles (Extended Data Fig. 3), showing that the FET structure is crucial for high sensitivity: low doping (LD, uniform doping at ~$10^7\,\Omega\,sq^{-1}$ in the silicon-on-insulator substrate), selective doping (SD, light doping at ~$10^4\,\Omega\,sq^{-1}$ in the gate and heavy doping in the drain and source) and heavy doping (HD, uniform doping at ~$10^2\,\Omega\,sq^{-1}$). **c**, Output characteristics of the n-channel FET in the linear region under different applied gate voltages (i) and transfer characteristics of the FET under different drain voltages (ii). The FET is in depletion mode, which is 'ON' at zero gate voltage. It shows a high transconductance in the ~100 to 100 mV regime. V_d, drain voltage; V_g, gate voltage. **d**, Output (i) and transfer (ii) characteristics of each FET in a 10-FET array. The insets show the distribution of the FET conductance (i) and transconductance (ii). **e**, Comparison of the 10-FET array's conductance (i) and transconductance (ii) before and after compressive buckling, illustrating that the buckling process has no impact on the FET's electrical performance. The circles and error bars show the mean and standard deviation of the FETs' properties, respectively. **f**, Comparison of the FETs' electrical conductance with and without saline solution on the gate terminal, showing minimal current leakage of the FETs. The circles and error bars show the mean and standard deviations of the FETs' properties. The ionic solution induces slightly more carriers (due to surface-adsorbed H^+), and thus slightly higher conductance in the conduction channel. **g**, Temporal response of the FETs to gate signals. A 100 mV pulse (rising/falling (R/f) time 0.1 ms, duration 1 ms, green curve) was applied to the gate, and the corresponding conductance of the FET (black curve) shows changes coincident with the input signal without any noticeable delay (i). Ten repeated characterizations of the same FET with an input gate signal at the sampling rate of 100 kHz (0.01 ms resolution) shows no observable jitter (<0.01 ms) in the data acquisition system (ii). The FET's conductance is reliable and independent of the rising/falling times of the input signals (iii).

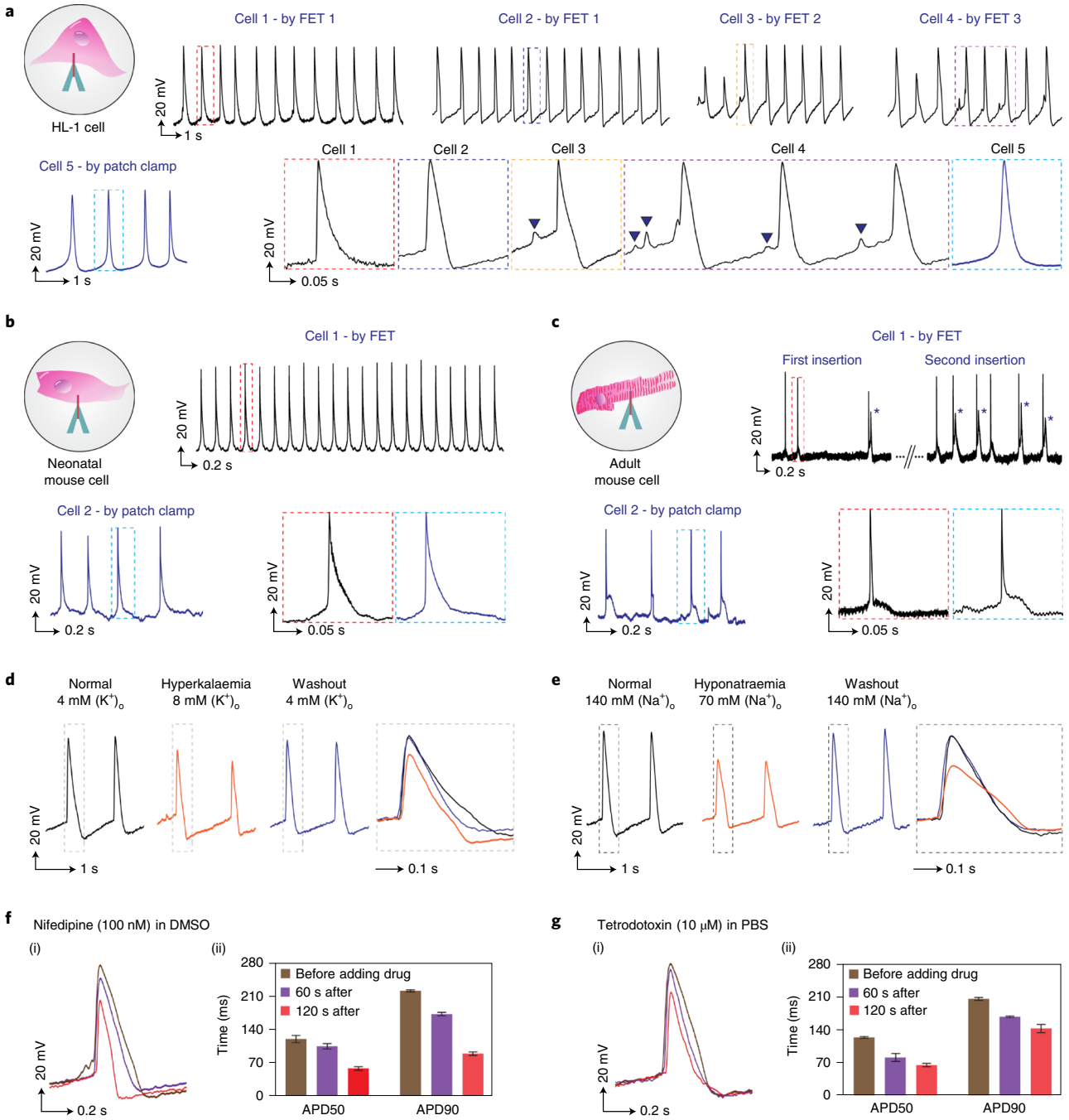

Fig. 3 | Intracellular recordings and validations on single cardiomyocytes. a, Periodic spikes can be recorded from different HL-1 cells by different FETs (top). The results are validated using the whole-cell patch clamp (lower left). The enlarged regions of the recordings by the FETs and the patch clamp (highlighted by boxes) represent typical pacemaker action potentials of the HL-1 cells (lower right). The mean of the action potentials measured by the FETs is 121.4 ± 1.3 mV, which is close to the 122.0 ± 4.0 mV measured by the patch clamp, showing the FETs' capability for recording full-amplitude action potentials. Subthreshold signals (for example, cell membrane oscillations of 5–15 mV) are captured in the recordings of cells 3 and 4, as highlighted by the black triangles. **b**,**c**, Intracellular recordings from primary cells including neonatal mouse atrial cardiomyocytes (**b**) and adult mouse ventricular cardiomyocytes (**c**). The greater noise in **c** is induced by the contraction of the adult mouse cells during measurements. In some spikes in **c**, an upstroke can be observed during repolarization, as marked by the asterisks, indicating abnormal Ca^{2+} influxes, which are also likely caused by the contraction. **d**,**e**, Pathological studies of the HL-1 cells by modulating potassium ion (**d**) and sodium ion (**e**) concentrations in the culture solutions (that is, solutions outside of the cell membrane, ion concentrations were labelled by $[K^+]_o$ and $[Na^+]_o$. Both the hyperkalaemia cells (**d**) and the hyponatraemia cells (**e**) exhibit a decreased signal amplitude, a shortened action potential duration and a longer refractory period compared with the normal cells, as recorded by the FET. The recorded action potentials recover when the culture solutions are switched back to Tyrode's solution. **f**,**g**, Effects of the ion channel blocking drugs nifedipine (**f**) and tetrodotoxin (**g**) on the action potential morphologies of HL-1 cells recorded by the FET (i) and the corresponding quantitative analysis (ii). Cells exposed to 100 nM nifedipine exhibit a lower spike amplitude and shorter APD50 and APD90. The cells repolarize very quickly because nifedipine is an L-type Ca^{2+} channel blocker, which diminishes the influx of Ca^{2+} into the cells. Tetrodotoxin (10 μM) acts on the rapid Na^+ channels, reducing the spike amplitude and thus shortening the repolarization duration. The colour code in **f**,**g**(ii) applies to **f**,**g**(i). The error bars represent standard deviations of 20 recorded action potentials. DMSO, dimethylsulfoxide; PBS, phosphate-buffered saline.

We tested the FET performance by verifying the HL-1 cells' response to extracellular solution composition and ion channel blocking drugs. Figure 3d,e shows the effect of hyperkalaemia or hyponatraemia on the recorded electrophysiological behaviours of cardiomyocytes, including the beating rhythm, resting membrane potential and action potential duration. Abnormally high potassium or low sodium ion concentration would vary the cell's action potential shape by shortening the duration and decreasing the amplitude[28,29]. Figure 3f,g shows the measured responses of HL-1 cells to ion channel blockers with modulated action potential amplitude and duration. The results show that nifedipine or tetrodotoxin lowers the amplitude and reduces the action potential duration (APD) at 50 or 90% repolarization (APD50 or APD90; the data are listed in Supplementary Table 1). The effect was reversible, as revealed after the extracellular solution was swapped back to the normal composition.

Recording intercellular signal conductions

We used a 3D 10-FET array with well-defined spacing (Fig. 4a) to record intercellular signal conductions, which are related to the electrical coupling states between cells[30]. When a common electrical pulse was provided, the FETs exhibited the same characteristics and the electrical signal delay between any two channels was no greater than 0.01 ms, suggesting that the system-induced electrical delay was negligible (Supplementary Fig. 19). A layer of spontaneously firing HL-1 cells cultured on a polydimethylsiloxane (PDMS) sheet was laminated on the FET array (Fig. 4b; see Methods and Supplementary Figs. 4 and 20–23 for details). We used electrical stimulation to regulate the firing patterns of the HL-1 cells to study the direction and velocity of intercellular signal conduction. Four electrodes were placed in the four corners of the cell culture, and a stimulation pulse was applied to one electrode in each measurement (Fig. 4c). Under electrical pacing, spontaneous arrhythmic action potentials were suppressed[31], and the corresponding recorded cellular signals are shown in Fig. 4d, Supplementary Fig. 24 and Extended Data Fig. 5. We calculated the signal latencies between the FETs by cross-correlating the recorded action potential profiles (Supplementary Fig. 25 and Supplementary Table 2). The heat map in Fig. 4d visualizes the action potential conduction direction among the cells, as indicated by the arrows. Based on the conduction latencies and the predefined distances between the FETs, the intercellular signal conduction velocity was calculated to be 35.1–39.3 $\mu m\,ms^{-1}$, comparable to the results from other studies on HL-1 cells[32]. Long-period recordings showed the robustness of the measurements by the FET array (Supplementary Fig. 26 and Supplementary Table 3).

Fast signal conductions within a cell

Intracellular signal conduction in cardiomyocytes corresponds to various forms of subcellular ionic activities[33]. However, it is challenging to record intracellular conductions in cardiomyocytes because it is difficult to interface two or more patch clamps with one cardiomyocyte[34]. Also, the short signal latency inside the cardiomyocyte can be overshadowed by the intrinsic delay of the existing recording systems[35].

In Fig. 4d, regardless of the orientation of the stimulation electrode, we found the latencies between the FETs at (2,3) and (1,3) to be always in the range 0.10–0.20 ms (Supplementary Table 2), which is much shorter than those between the other FETs. Given the distance between these two FETs (26.6 μm), the conduction velocity was calculated to be 182 $\mu m\,ms^{-1}$, which is about five times the intercellular conduction velocity (Fig. 4e). To verify the measurement, we used the same 10-FET array to study a different HL-1 cell culture. This time, we found no signal conduction between the FETs at (2,3) and (1,3), but two other FETs, at (1,1) and (1,2), showed a latency of ~0.18 ms (Supplementary Figs. 27c,d). To triple check the measurements, we used confocal microscopy to image live cells while simultaneously recording electrical signals. The results verified that two FETs were in the same cell (Fig. 4f and Supplementary Fig. 28). Therefore, the signals we measured between these two FETs are intracellular conductions. The slight fluctuation in the intracellular conduction velocity may be because of the constantly changing ionic distributions within the cell. The intracellular conduction is much faster than the intercellular conduction because the latter is slowed by ion diffusion processes via gap junctions between neighbouring cells[36].

Additionally, in Fig. 4d, when the stimulation originated from different orientations relative to the FETs, the corresponding intercellular signal conduction direction would change. However, we found that the intracellular conduction direction was always from (1,3) to (2,3), independent of the direction of intercellular conduction, which is probably related to the positions of the FETs and the coupling of cells with neighbouring cells (Supplementary Figs. 27e,f and 29). In other measurements, the intracellular conduction direction was reversed with different stimulation orientations (Supplementary Fig. 27e,f).

Intracellular recording of 3D tissue constructs

Compared with 2D cellular cultures, 3D engineered tissue constructs better resemble natural organs in structural complexity and physiological functions. Therefore, they are excellent models for intracellular electrophysiology studies[37]. However, existing devices have limitations in interfacing with 3D tissues: either they can only perform extracellular sensing[38], or they have a uniform height suitable for interrogating cells on a common plane only[24,25].

With tunable heights, the 3D FET array provides a unique opportunity to study the electrophysiology of 3D tissues. To this end, we fabricated a stretchable 128-FET array distributed in 40 units of three different heights, capable of interrogating cells at three different depths in a 3D microtissue (Fig. 5a and Supplementary Figs. 30–34). Representative recordings by the array showed intracellular action potentials in a 3D cardiac tissue, with 44% of the FETs being intracellular, 34% extracellular and 22% inactive, the intra- or extracellular signals being defined by the shape and amplitude of the signals[39] (Fig. 5b,c). The inactive FETs could be due to electrically inactive cells, degraded performance of the FET or non-ideal FET–cell coupling (for example, because of an elastic response from the cytoskeleton).

We used the FETs in each unit to study the small-scale intercellular signal conductions, whose velocities were calculated to be $18.8 \pm 7.5\,\mu m\,ms^{-1}$, consistent with reported values[25] (Fig. 5d and Extended Data Fig. 6). We also leveraged the relatively large spacing between the 40 units of the FETs to determine the velocity of large-scale signal conduction (Fig. 5e). For each of the three heights, the signals propagate clockwise among the units, forming a loop (Fig. 5e). The signal conduction velocities in the three different loops were calculated to be 10.9, 11.8 and 12.2 $\mu m\,ms^{-1}$ (Fig. 5f). The calculated large-scale conduction velocities are generally lower than the small-scale velocities within each unit, because we assume the signal conduction path is linear from point to point on the large scale, whereas the actual path is likely to follow a zig-zag pattern[25], depending on the relative positions of the cells and their electrical coupling states.

Conclusions

With the device size down to the submicrometre regime, the high sensitivity and the high signal-to-noise ratio, FETs have attracted growing attention in the last decade as a tool for interrogating electrogenic cells. Two-dimensional planar FETs for extracellular interfacing usually lack one-to-one correspondence between the cells and FETs, providing information on an ensemble of cells near the FET. Three-dimensional FETs allow direct interfacing

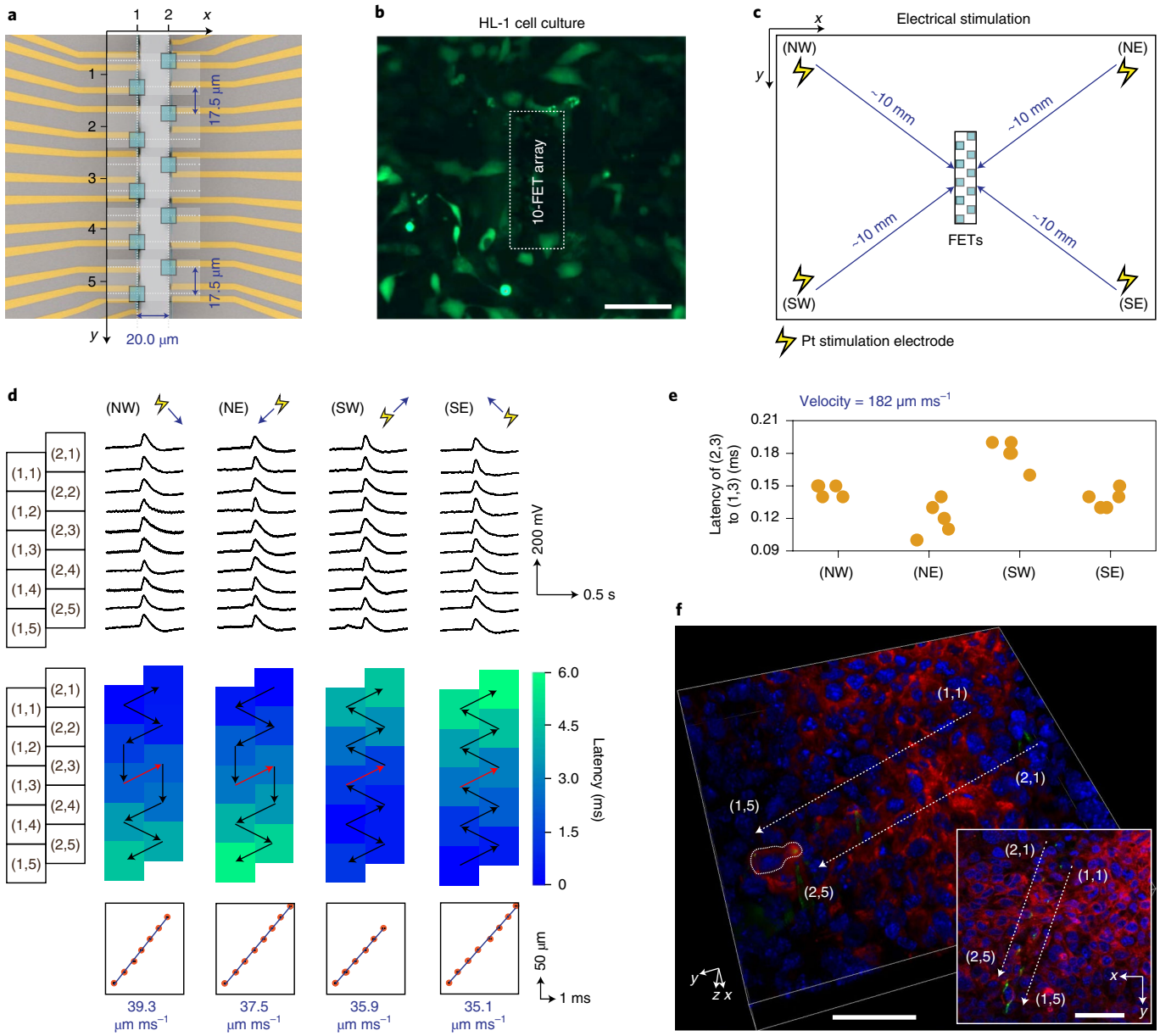

Fig. 4 | Intracellular recording of a 2D HL-1 cell culture by a 10-FET array. a, Schematic top view of a 10-FET array. The spacing between each FET was accurately defined by lithography. A coordinate system is used to denote the position of each FET, indicated by the green squares. **b**, A fluorescent image of a 10-FET array interfacing with a 2D culture of HL-1 cells (average size ~50 μm), stained by Fluo-4 AM dye. During the measurement, only the FETs are interfacing the cells, while the areas around them are not contacting them. Scale bar, 100 μm. **c**, Schematic of the set-up for stimulating the HL-1 cells, with four Pt electrodes placed in four corners of the cell culture. A stimulation pulse was applied to a single electrode in each measurement. We used biphasic pulses, so the net injection current was zero. The frequency, width and amplitude of the pulses were 1 Hz, 1 ms and 1 V, respectively, to effectively pace the cells. **d**, Simultaneous intracellular recordings from a 2D HL-1 cell culture under electrical pacing at different orientations to the FETs (top). All FETs recorded periodic intracellular action potentials of 95–116 mV (Extended Data Fig. 5). Heat maps illustrate the latency of the action potentials among the cells (middle). The arrows indicate the possible signal conduction paths between the cells; the black arrows show intercellular signal conductions and the red arrows show intracellular signal conductions. In all measurements, the signal first arrives at the cell closest to the stimulation electrode and then transmits to the neighbouring cells. The average intercellular conduction velocity is 35.1–39.3 μm ms^{-1} (bottom). Regardless of the stimulation orientation to the FETs, the intracellular signal conduction is always from (1,3) to (2,3). **e**, The average latency between (1,3) and (2,3) calculated from the 20 action potentials in four orientations is 0.146 ± 0.025 ms. The intracellular conduction velocity is 182 μm ms^{-1}, which is about five times the velocity of intercellular conduction. **f**, Confocal microscopy image illustrating a 3D view of FETs intracellularly interfacing live HL-1 cells. The inset shows the corresponding top view. Green (rhodamine 6G), the PI in the FETs; red (CellBrite), cell membranes; blue (NucBlue), cell nuclei. The images clearly show that two FETs, (1,5) and (2,5), are interfacing the same cell. The corresponding action potential recordings are presented in Supplementary Fig. 28d. Scale bars, 50 μm.

with the cytoplasm of cells, which ensures correspondence with each specific recorded cell. However, existing 3D FET devices are not suited to large-scale, high-spatial-resolution sensing[8]. With an unprecedented number of FETs and a predefined layout, the 3D FET array demonstrated in this work can fill this technological gap (Supplementary Fig. 35).

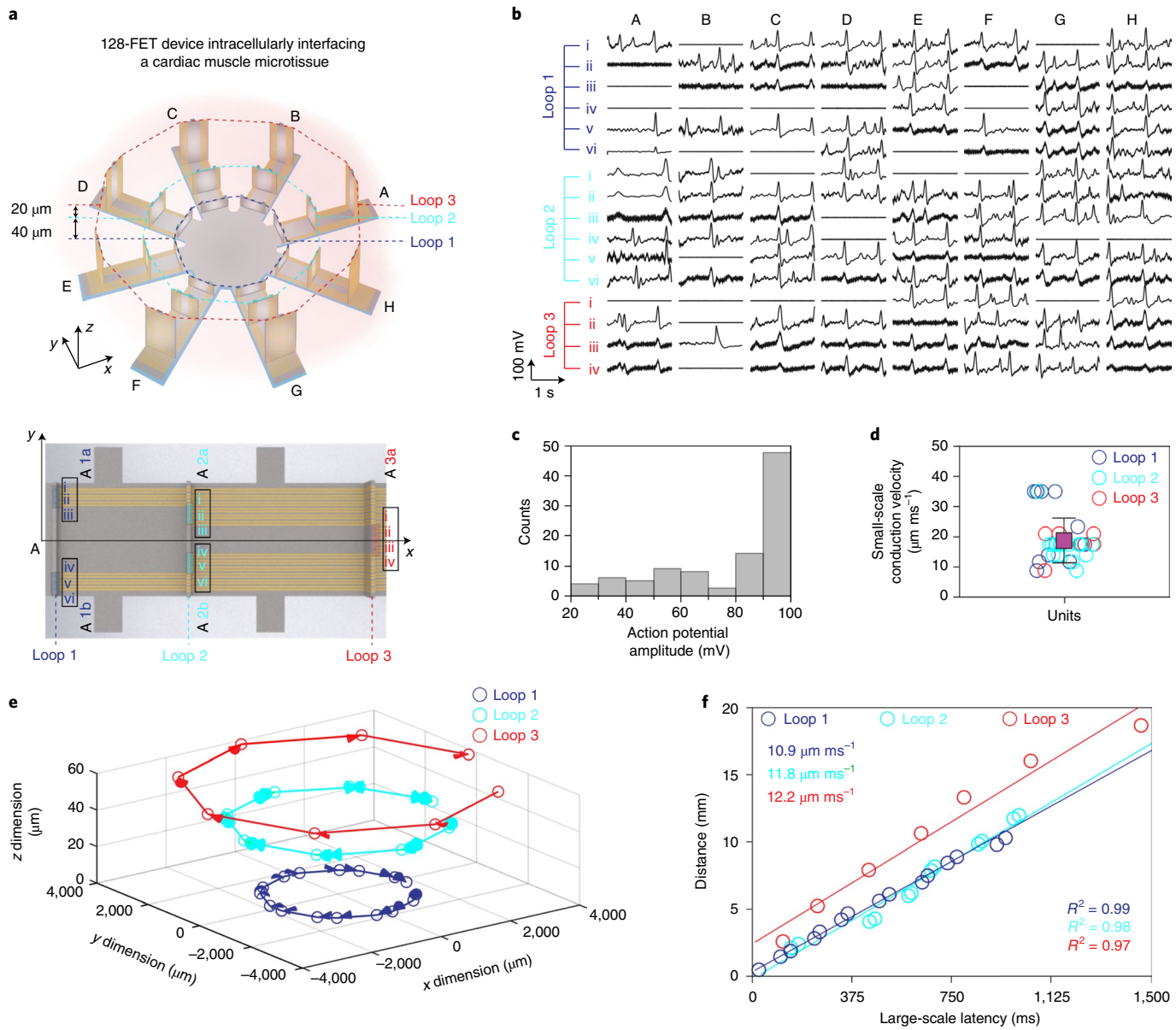

Fig. 5 | Intracellular recording of a microtissue of neonatal rat cardiomyocytes using a 128-FET array. a, Schematic diagrams of the 128-FET array distributed on eight arms. On each arm, there are 16 FETs in five units of different heights, distributed in three concentric loops (top). The relative positions of the 16 FETs and their coordinates are indicated (bottom). **b**, Representative recordings from the 3D cardiac tissue by the 128-FET array. Intracellular action potentials are recorded from all three loops on each arm. **c**, A histogram of the spike amplitudes in **b**. **d**, The small-scale intercellular signal conduction velocity measured within each unit. The average velocity (purple square) within the 40 units is $18.8 \pm 7.5\,\mu m\,ms^{-1}$. **e**, Three-dimensional visualization of the signal conduction in the whole 3D tissue construct. The signal conduction directions are consistent in all three loops, beginning at arm H and then propagating to arm A. **f**, Linear fit of the intercellular signal conduction velocity across the units in each loop.

The arrayed FETs provide tremendous opportunities for studying the fundamental physiologies of electrogenic cells. The acquired knowledge can help to understand the pathology and guide the treatment of numerous evolutionary disease models[40]. Intracellular signals disclose more meaningful information about the cell type and density of various ion channels[1,2]. In particular, full-amplitude action potentials are highly relevant to the disease status and pathology of cells[41]. Subthreshold signals can potentially shed light on the process of intercellular synchronization[42], the mechanism of electrophysiological modulation[20,43] and how these subthreshold signals impact the development of sensory systems[44]. Studies of the conduction behaviour would not only enhance the understanding of the ionic transport across organellular membranes within a cell[45], but also facilitate the study of electrical coupling between different cells[36]. These findings have important implications for understanding subcellular electrophysiology, organellar ionic dynamics[45], organelle–cell membrane interaction[46] and their influences on cellular physiological activities, including proliferation, differentiation and apoptosis[47].

Further explorations could follow by applying the 3D FET array to various types of cardiac tissues, such as embryonic stem cell-derived cardiomyocytes, myocyte–fibroblast cocultures and other general electrogenic cells, such as neurons. Reliable recordings of 3D tissues on a large scale may reveal cellular alignment directions. Future translation of this platform technology to in vivo studies will depend on the FET's ability to penetrate through the

thick membranes of the myocardium and the cortex, prevent severe immune responses and eliminate motion artifacts induced by heart beating and brain pulsation. To that end, further refinement of the 3D FET structure (for example, tip size, spacing and relative positions), array size, structural materials, surface coating and deployment approach, as well as the use of artificial intelligence-assisted signal processing, would be essential to enhance the reliability, quality and duration of the recordings.

Online content

Any methods, additional references, Nature Research reporting summaries, source data, extended data, supplementary information, acknowledgements, peer review information; details of author contributions and competing interests; and statements of data and code availability are available at https://doi.org/10.1038/s41565-021-01040-w.

Received: 8 June 2021; Accepted: 27 October 2021;
Published online: 23 December 2021

References

1. Kim, D. H. et al. Dissolvable films of silk fibroin for ultrathin conformal bio-integrated electronics. *Nat. Mater.* **9**, 511–517 (2010).
2. Abbott, J. et al. A nanoelectrode array for obtaining intracellular recordings from thousands of connected neurons. *Nat. Biomed. Eng.* **4**, 232–241 (2020).
3. Dai, X. et al. Three-dimensional mapping and regulation of action potential propagation in nanoelectronics-innervated tissues. *Nat. Nanotechnol.* **11**, 776–782 (2016).
4. Tian, B. et al. Three-dimensional, flexible nanoscale field-effect transistors as localized bioprobes. *Science* **329**, 830–834 (2010).
5. Jiang, Y. et al. Heterogeneous silicon mesostructures for lipid-supported bioelectric interfaces. *Nat. Mater.* **15**, 1023–1030 (2016).
6. Wang, X. & Li, M. Automated electrophysiology: high throughput of art. *Assay Drug Dev. Technol.* **1**, 695–708 (2003).
7. Fast, V. G. & Kléber, A. G. Microscopic conduction in cultured strands of neonatal rat heart cells measured with voltage-sensitive dyes. *Circ. Res.* **73**, 914–925 (1993).
8. Hong, G. & Lieber, C. M. Novel electrode technologies for neural recordings. *Nat. Rev. Neurosci.* **20**, 330–345 (2019).
9. Zhang, X. Nanowires pin neurons: a nano "moon landing". *Matter* **1**, 560–562 (2019).
10. Aranega, A., de la Rosa, A. & Franco, D. Cardiac conduction system anomalies and sudden cardiac death: insights from murine models. *Front. Physiol.* **3**, 211 (2012).
11. Xu, S. et al. Assembly of micro/nanomaterials into complex, three-dimensional architectures by compressive buckling. *Science* **347**, 154–159 (2015).
12. Tian, B. & Lieber, C. M. Nanowired bioelectric interfaces. *Chem. Rev.* **119**, 9136–9152 (2019).
13. Fan, J. A. et al. Fractal design concepts for stretchable electronics. *Nat. Commun.* **5**, 3266 (2014).
14. Khang, D. Y., Jiang, H., Huang, Y. & Rogers, J. A. A stretchable form of single-crystal silicon for high-performance electronics on rubber substrates. *Science* **311**, 208–212 (2006).
15. Schaefer, N. et al. Multiplexed neural sensor array of graphene solution-gated field-effect transistors. *2D Mater.* **7**, 025046 (2020).
16. Lee, J. W. et al. Analysis of charge sensitivity and low frequency noise limitation in silicon nanowire sensors. *J. Appl. Phys.* **107**, 044501 (2010).
17. Rettinger, J., Schwarz, S. & Schwarz, W. Electrophysiology (Springer, 2016).
18. Noy, A. Bionanoelectronics. *Adv. Mater.* **23**, 807–820 (2011).
19. Hempel, F. et al. PEDOT:PSS organic electrochemical transistor arrays for extracellular electrophysiological sensing of cardiac cells. *Biosens. Bioelectron.* **93**, 132–138 (2017).
20. Grant, A. O. Cardiac ion channels. *Circ. Arrhythm. Electrophysiol.* **2**, 185–194 (2009).
21. Duan, X. et al. Intracellular recordings of action potentials by an extracellular nanoscale field-effect transistor. *Nat. Nanotechnol.* **7**, 174–179 (2011).
22. Gong, H. et al. Biomembrane-modified field effect transistors for sensitive and quantitative detection of biological toxins and pathogens. *ACS Nano* **13**, 3714–3722 (2019).
23. Qing, Q. et al. Free-standing kinked nanowire transistor probes for targeted intracellular recording in three dimensions. *Nat. Nanotechnol.* **9**, 142–147 (2014).
24. Zhao, Y. et al. Scalable ultrasmall three-dimensional nanowire transistor probes for intracellular recording. *Nat. Nanotechnol.* **14**, 783–790 (2019).
25. Abbott, J. et al. CMOS nanoelectrode array for all-electrical intracellular electrophysiological imaging. *Nat. Nanotechnol.* **12**, 460–466 (2017).
26. Xie, C. et al. Intracellular recording of action potentials by nanopillar electroporation. *Nat. Nanotechnol.* **7**, 185–190 (2012).
27. Elcarpio, J. O. B. D. et al. HL-1 cells: a cardiac muscle cell line that contracts and retains phenotypic characteristics of the adult cardiomyocyte. *Proc. Natl Acad. Sci. USA* **95**, 2979–2984 (1998).
28. Hegyi, B., Chen-Izu, Y., Izu, L. T. & Bányász, T. Altered K^+ current profiles underlie cardiac action potential shortening in hyperkalemia and β-adrenergic stimulation. *Can. J. Physiol. Pharmacol.* **97**, 773–780 (2019).
29. Lu, Y.-Y. et al. Electrolyte disturbances differentially regulate sinoatrial node and pulmonary vein electrical activity: a contribution to hypokalemia- or hyponatremia-induced atrial fibrillation. *Heart Rhythm* **13**, 781–788 (2016).
30. Robinson, J. T. et al. Vertical nanowire electrode arrays as a scalable platform for intracellular interfacing to neuronal circuits. *Nat. Nanotechnol.* **7**, 180–184 (2012).
31. Czeschik, A. et al. Nanostructured cavity devices for extracellular stimulation of HL-1 cells. *Nanoscale* **7**, 9275–9281 (2015).
32. Kireev, D. et al. Graphene multielectrode arrays as a versatile tool for extracellular measurements. *Adv. Healthc. Mater.* **6**, 1601433 (2017).
33. Bers, D. M., Barry, W. H. & Despa, S. Intracellular Na^+ regulation in cardiac myocytes. *Cardiovasc. Res.* **57**, 897–912 (2003).
34. Brown, A. M., Lee, K. S. & Powell, T. Voltage clamp and internal perfusion of single rat heart muscle cells. *J. Physiol.* **318**, 455–477 (1981).
35. Gouwens, N. W. & Wilson, R. I. Signal propagation in *Drosophila* central neurons. *J. Neurosci.* **29**, 6239–6249 (2009).
36. McCain, M. L. et al. Cell-to-cell coupling in engineered pairs of rat ventricular cardiomyocytes: relation between Cx43 immunofluorescence and intercellular electrical conductance. *Am. J. Physiol. Heart Circ. Physiol.* **302**, H443–H450 (2012).
37. Lancaster, M. A. & Knoblich, J. A. Organogenesis in a dish: modeling development and disease using organoid technologies. *Science* **345**, 1247125 (2014).
38. Hong, G. et al. A method for single-neuron chronic recording from the retina in awake mice. *Science* **360**, 1447–1451 (2018).
39. Dipalo, M. et al. Intracellular and extracellular recording of spontaneous action potentials in mammalian neurons and cardiac cells with 3D plasmonic nanoelectrodes. *Nano Lett.* **17**, 3932–3939 (2017).
40. Nattel, S. Electrical coupling between cardiomyocytes and fibroblasts: experimental testing of a challenging and important concept. *Cardiovasc. Res.* **114**, 349–352 (2018).
41. Lin, Z. C. et al. Accurate nanoelectrode recording of human pluripotent stem cell-derived cardiomyocytes for assaying drugs and modeling disease. *Microsyst. Nanoeng.* **3**, 16080 (2017).
42. Desmaisons, D., Vincent, J.-D. & Lledo, P.-M. Control of action potential timing by intrinsic subthreshold oscillations in olfactory bulb output neurons. *J. Neurosci.* **19**, 10727–10737 (1999).
43. Frohnwieser, B., Chen, L. Q., Schreibmayer, W. & Kallen, R. G. Modulation of the human cardiac sodium channel alpha-subunit by cAMP-dependent protein kinase and the responsible sequence domain. *J. Physiol.* **498**, 309–318 (1997).
44. Boehmer, G., Greffrath, W., Martin, E. & Hermann, S. Subthreshold oscillation of the membrane potential in magnocellular neurones of the rat supraoptic nucleus. *J. Physiol.* **526**, 115–128 (2000).
45. Kamiya, K. et al. Electrophysiological measurement of ion channels on plasma/organelle membranes using an on-chip lipid bilayer system. *Sci. Rep.* **8**, 17498 (2018).
46. Li, J. et al. Scanning microwave microscopy of vital mitochondria in respiration buffer. In *Proc. 2018 IEEE MTT-S International Microwave Symposium* 115–118 (IEEE, 2018).
47. Moon, C. H. et al. KR-31378, a novel benzopyran analog, attenuates hypoxia-induced cell death via mitochondrial K_{ATP} channel and protein kinase C-ε in heart-derived H9c2 cells. *Eur. J. Pharmacol.* **506**, 27–35 (2004).

Publisher's note Springer Nature remains neutral with regard to jurisdictional claims in published maps and institutional affiliations.

© The Author(s), under exclusive licence to Springer Nature Limited 2021

Methods

The materials, software/algorithms and equipment are listed in the Supplementary Information.

Fabrication of the 3D FETs. The FET arrays were fabricated by the compressive buckling technique. The 2D structure contained silicon FETs, gold electrodes prepared by sputtering, two PI layers and an SU-8 mechanical supporting layer obtained by spin casting. The shapes and patterns of each layer were defined by lithography and reactive ion etching. The overall fabrication process included four main steps. In a nutshell, the FET was first prepared on a silicon-on-insulator wafer by standard cleanroom micro/nanofabrication techniques. Second, the completed FET was released from the silicon-on-insulator wafer and transfer-printed onto a temporary 2D substrate. Third, different functional materials were sequentially deposited onto the FET to enable the electrical and mechanical robustness of the device. Finally, the fabricated multilayered device was released and transfer-printed onto a prestrained elastomeric substrate for controlled buckling. The fabrication process is described in detail in Fig. 1, Extended Data Fig. 1 and Supplementary Note 1.

Finite element analysis of the 3D FET. ABAQUS (v.6.13, Dassault Systèmes Simulia Corp.) was used to study the mechanical behaviour of the device during compressive buckling. As the thickness of the silicone substrate was much greater than that of the device, a boundary condition was to constrain the device to buckle only above the substrate. Displacement boundary conditions were applied to the two edges of the device to initiate the compression. Composite shell elements (S4R) were used to model the SU-8, PI, Si and Au layers. The minimal size of the element was set to be half of the FET tip's width (~0.5 μm). The total number of elements in the model was ~106. Mesh convergence of the simulation was accomplished in all cases. The elastic moduli (E) and Poisson's ratios (ν) of the different layers are as follows: $E_{PI}=2.5$ GPa, $\nu_{PI}=0.34$; $E_{Si}=130$ GPa, $\nu_{Si}=0.27$; $E_{Au}=78$ GPa, $\nu_{Au}=0.44$; $E_{SU\text{-}8}=4$ GPa, $\nu_{SU\text{-}8}=0.22$. The fracture strains of Au and Si are 5 and 1%, respectively[14,15].

Surface conductivity mapping of the FET. The FET was characterized using a scanning microwave microscope (KeysightTM 7500), which combined an atomic force microscope and a vector network analyser. The atomic force microscope had a conductive probe that scanned the FET surface, revealing the topography. Simultaneously, a microwave signal from the network analyser was transmitted to the probe, reflected by the sample at the contact point and then sent back to the network analyser. The conductance information was obtained from the reflection coefficient, determined from the transmission and reflection signals. The reflection coefficient calculations are presented in Supplementary Note 2.

Phospholipid coating. Phospholipid coating of the FET surface facilitated the cell internalization process, through spontaneous fusion, to achieve direct contact with the cell cytosol. Briefly, large phospholipid vesicles in aqueous solutions were broken into small unilamellar vesicles by consecutive freeze-and-thaw treatments, sonication and filter extrusion. These high-surface-energy vesicles formed a uniform phospholipid coating on the FET surface by self-assembly. The schematics in Supplementary Fig. 7 and Supplementary Note 9 demonstrate the whole process. Successful coating of the phospholipids was verified by fluorescent imaging (Supplementary Fig. 8).

Fabrication of the multi-electrode array. The multi-electrode array (MEA), composed of Au electrodes, an SU-8 insulation layer and a glass substrate, was fabricated using standard micro/nanofabrication techniques. The fabrication process is described in detail in Supplementary Note 11.

Water-gate characterization. FET sensitivity was determined by measuring the FET transfer characteristics. In the water-gate characterization (Supplementary Fig. 4), the corresponding FET conductance was measured under a fixed positive bias (for example, 200 mV) at the source and a potential sweep (from −100 to 100 mV) at the gate. Experimental details are provided in Supplementary Note 6.

Ca^{2+} sparks screening. The schematics in Supplementary Fig. 10 illustrate the process of staining Ca^{2+} and monitoring their transient activity under a fluorescent microscope. First, the HL-1 cells were cultured in supplemented Claycomb medium. We then removed the cell culture medium by aspiration and added typical clear-colour Tyrode's solution. Second, we added Fluo-4 AM (InvitrogenTM) stock solution to the cells and incubated them for 1 h to facilitate the loading of calcein dyes. Then, we removed the old solution and refilled it with fresh Tyrode's solution. Finally, we monitored the Ca^{2+} signals under a microscope with a 480 nm excitation filter and a 525 nm emission filter.

HL-1 cell culture. We followed the standard cell culture protocol provided by Sigma-Aldrich. All materials and solutions were from Sigma-Aldrich. The cells were cultivated in supplemented Claycomb medium after precoating the substrates with templating materials. We prepared the cell cultures on PDMS sheets for signal recording, in cell culture flasks for cell proliferation and on cell culture dishes for Ca^{2+} sparks screening. The details are provided in Supplementary Note 7.

Primary cardiomyocytes culture. Neonatal mouse ventricular myocytes were isolated from 1- to 2-day-old Black Swiss mouse pups purchased from Charles Rivers Laboratories. Adult mouse single ventricular myocytes were isolated from mouse ventricles using Langendorff's enzymatic digestion method. The cells were obtained by digesting the ventricles in buffered solutions. After removing the fibroblast cells and blood from the vasculature, the cardiomyocytes were cultured on laminin-templated PDMS sheets or cell culture dishes for signal recording. The preparation of the solutions is described in detail in Supplementary Note 8.

Whole-cell patch clamp electrophysiology. Whole-cell current patching of HL-1 cells and primary cardiomyocytes was performed at 35 °C with cells plated on a PDMS sheet superfused with an external solution. A glass micropipette that was filled with the solution in its lumen was attached to the cell membrane, forming a gigaseal between the micropipette and the cell membrane. After that, the membrane patch was ruptured by a negative pressure in the pipette, which established the whole-cell configuration. Action potentials were recorded with a holding potential of −80 to −40 mV, and evoked by injecting currents into the cells. More information is provided in Supplementary Note 12.

Data acquisition. An electrophysiological signal acquisition system includes the FETs for interfacing the cells, preamplifiers, a signal digitizer and a graphical user interface (that is, computer software) for data visualization. We used a customized 10-channel preamplifier and a commercial data acquisition system and software (Axon) with the 10-FET array, and a commercial 256-channel current-input analogue-to-digital converter (Texas Instruments) and its configured software with the 128-FET array. The sampling rates adopted in these recordings ranged from 500 to 100,000 Hz in the different systems. Before recording cellular signals, we characterized the complete signal measurement system (including a 10-FET array, the preamplifier and the data acquisition device) and confirmed that the system had low intrinsic noise and no electrical crosstalk between the channels (Supplementary Figs. 22 and 23). More information is provided in Supplementary Note 13.

Signal processing. All signal recordings were post-processed offline in MATLAB (MathWorks). The intracellular and extracellular signals of 2D cell cultures (HL-1 cells, adult and neonatal mouse cardiomyocytes) recorded by the FETs had high signal-to-noise ratios and thus the raw data are presented. The MEA recordings of HL-1 cells were passed through a notch filter (60 Hz) and a bandpass filter (0.5–30 Hz). The electrical signals of the 3D cardiac muscle tissues, unless specified otherwise, were filtered through a bandpass filter (0.1–30 Hz). The FET sensitivity, noise level and delay between two action potential signals were also calculated in MATLAB (Supplementary Notes 3 and 14).

Electrical stimulation of the HL-1 cells. Platinum electrodes were used to stimulate the HL-1 cells and manipulate their firing patterns. We applied biphasic squared pulses (1 V, 1 Hz and 1 ms peak width) from an analogue output terminal of a commercial DAQ system (Digidata 1440, Axon) with commercial software (pCLAMP 10.3, Axon). The electrodes were placed ~10 mm away from the FETs.

Pharmacological and ion-concentration modulation of HL-1 cell electrophysiology. To explore the effects of drugs on cell electrophysiology we added channel blockers nifedipine (Sigma Aldrich or Abcam) or tetrodotoxin (Sigma Aldrich or Abcam) to typical Tyrode's solution. We also tuned the potassium or sodium concentration in the typical Tyrode's solution. The resulting solutions were administered by the perfusion (that is, simultaneously aspirating the old solution and adding the new solution) of cells. The electrical signals of the cells were recorded simultaneously. See Supplementary Note 15 for further discussions.

Engineering of cardiac microtissues. Neonatal rat cardiomyocyte tissues were engineered on a PDMS platform composed of a well and two microposts following the previously reported method[48] (Supplementary Fig. 34). Cardiomyocytes were mixed with collagen-based gel at a density of ~5×10^6 cells ml^{-1}. Each cell-laden hydrogel was added to the PDMS well around the two microposts and incubated for 1 h. Then, the culture medium was added to the cell-laden gels, followed by incubation. More details are provided in Supplementary Note 16.

Fluorescence staining of live cells. HL-1 cell membranes were marked with a cytoplasmic membrane dye (CellBrite), cell nuclei were stained with NucBlue and the PI layer in the FETs was mixed with rhodamine 6G dye. See Supplementary Note 17 for further discussions

Quantification and statistical analysis. The number of experiments and replicates is indicated in individual figure legends. The signal latencies in Fig. 4 were calculated by cross-correlating each two recording traces in MATLAB. The signal conduction velocities were calculated by linear regression of the signal latencies extracted from the raw data. The data presented in Figs. 2–5 were processed and visualized using MATLAB.

Reporting Summary. Further information on research design is available in the Nature Research Reporting Summary linked to this article.

Data availability

All data supporting the findings of this study are available within the paper and its Supplementary Information. The data generated in this study are available from Harvard Dataverse at https://dataverse.harvard.edu/dataset.xhtml?persistentId=doi:10.7910/DVN/7R0DQK&version=DRAFT. Source data are provided with this paper.

Code availability

The code that produced the findings of this study is available from the corresponding author upon reasonable request.

References

48. Zhao, Y. et al. A platform for generation of chamber-specific cardiac tissues and disease modeling. *Cell* **176**, 913–927.e18 (2019).

Acknowledgements

We thank H. Qian for discussing the cellular electrophysiology measurements taken using the patch clamp, J. Omens for discussing the electrophysiology recordings and electrical stimulation, R. Liu, L. Yan, Y. Luo and H. Ren for discussing the fabrication of the arrayed FETs, Y. Huo for analysing and discussing the characterization of Si doping, M. Makihata for discussing the design of the set-up for measuring the cellular signals, T. Pan for discussing the mechanical simulation, J. Zhao, X. Gao and Y. Wang for discussing data processing and analysis, N. Lawrence for discussing the immunofluorescent staining technique and S. Xiang for preparing the manuscript. This work was supported by the National Institutes of Health (1 R35 GM138250 01).

Author contributions

S.X., N.K. and Y.G. conceived the idea. S.X., N.K. and Y.G. designed the device. Y.G., N.K., Chunfeng Wang, J.Z., J.M. and Y. Li, fabricated the device. Y.G. and N.K. took the optical and SEM images. Y.G., N.K. and T.M.W. measured the signals with the patch clamp. Y.G., J.S., D.Z., J.M., A.Y. and L.H.-H.H. cultured the HL-1 cells. T.M.W. and J.S. isolated the primary cardiomyocytes of neonatal and adult mice. R.N., S.A. and A.K. prepared the microtissues of neonatal rat cardiomyocytes. J.L. and P.J.B. mapped the FET surface capacitance. Y.G. carried out the finite element analysis simulations. Y.G., N.K., Chunfeng Wang, J.Z. and Z.H. characterized the device electrically. Y.G., N.K., H.G., A.Y. and D.Z. coated the phospholipid on the FET device. Y.G., A.Y. and J.M. performed the fluorescent staining and confocal microscopy imaging. Y.G. fabricated the MEA. Y.G., J.S. and D.Z. carried out the Ca^{2+} sparks screening assays. Y.G. and D.Z. tested the viability of HL-1 cells. Z.L. and M.L. designed the 10-channel preamplifier. Y.G., Z.H. and W.L. designed the cellular signal measurement set-up. Y.G., Chunfeng Wang, N.K., J.Z. and W.L. measured and analysed the cellular signals. Y.G. and J.Z. drew the schematics and took photographs of the devices. Y.G. carried out the pharmacological and ion-concentration modulation of the HL-1 cells. Y.G. stimulated the HL-1 cells electrically. All authors contributed to discussions on the data and commented on the manuscript.

Competing interests

The authors declare no competing interests.

Additional information

Extended data is available for this paper at https://doi.org/10.1038/s41565-021-01040-w.

Supplementary information The online version contains supplementary material available at https://doi.org/10.1038/s41565-021-01040-w.

Correspondence and requests for materials should be addressed to Sheng Xu.

Peer review information *Nature Nanotechnology* thanks Xinyan Tracy Cui and Chi Hwan Lee for their contribution to the peer review of this work.

Reprints and permissions information is available at www.nature.com/reprints.

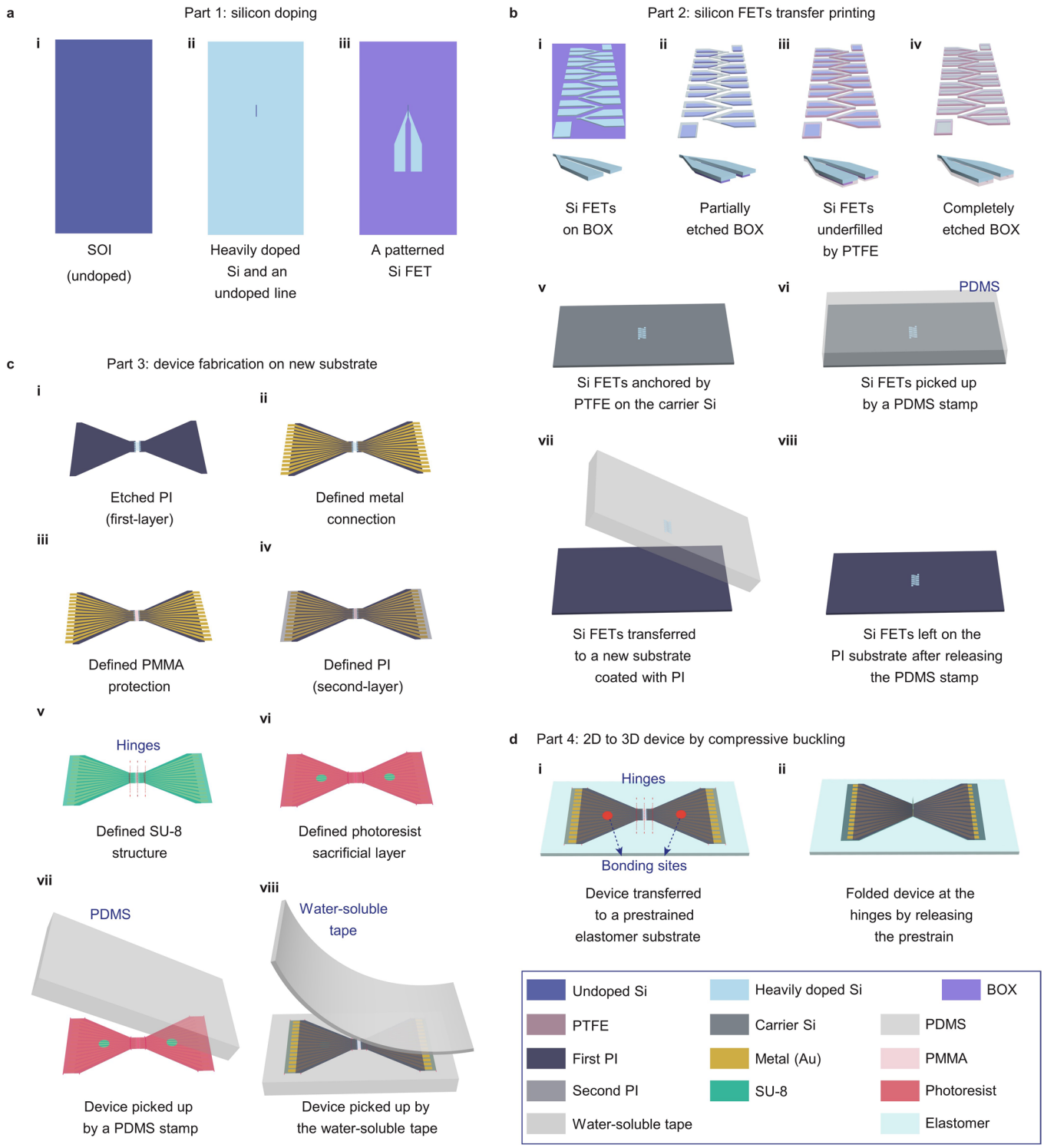

Extended Data Fig. 1 | Schematics illustrating the fabrication steps of the 3D FET array. a, The FET's drain, source, and gate regions are determined on an n-type SOI wafer by doping. First, the undoped region (that is, the region with only the background doping from the wafer) is coated by a layer of SiO_2 as the barrier for spin-on dopants from diffusing into the silicon substrate. Second, the FET shape is defined by photolithography and reactive ion etching. **b**, The FETs are firstly anchored to the substrate by PTFE, and then are transferred using a PDMS stamp to a temporary 2D substrate coated with PI. **c**, Multi-layered polymers and metal are coated and patterned on the temporary substrate. Finally, the layered device is transferred to a PDMS stamp and picked up by a water-soluble tape. **d**, The FET array is transferred to a prestrained elastomer substrate and selectively bonded at the two pre-designed bonding sites. When the prestrain releases, the 2D FET array gets compressed and buckled up to form 3D geometries.

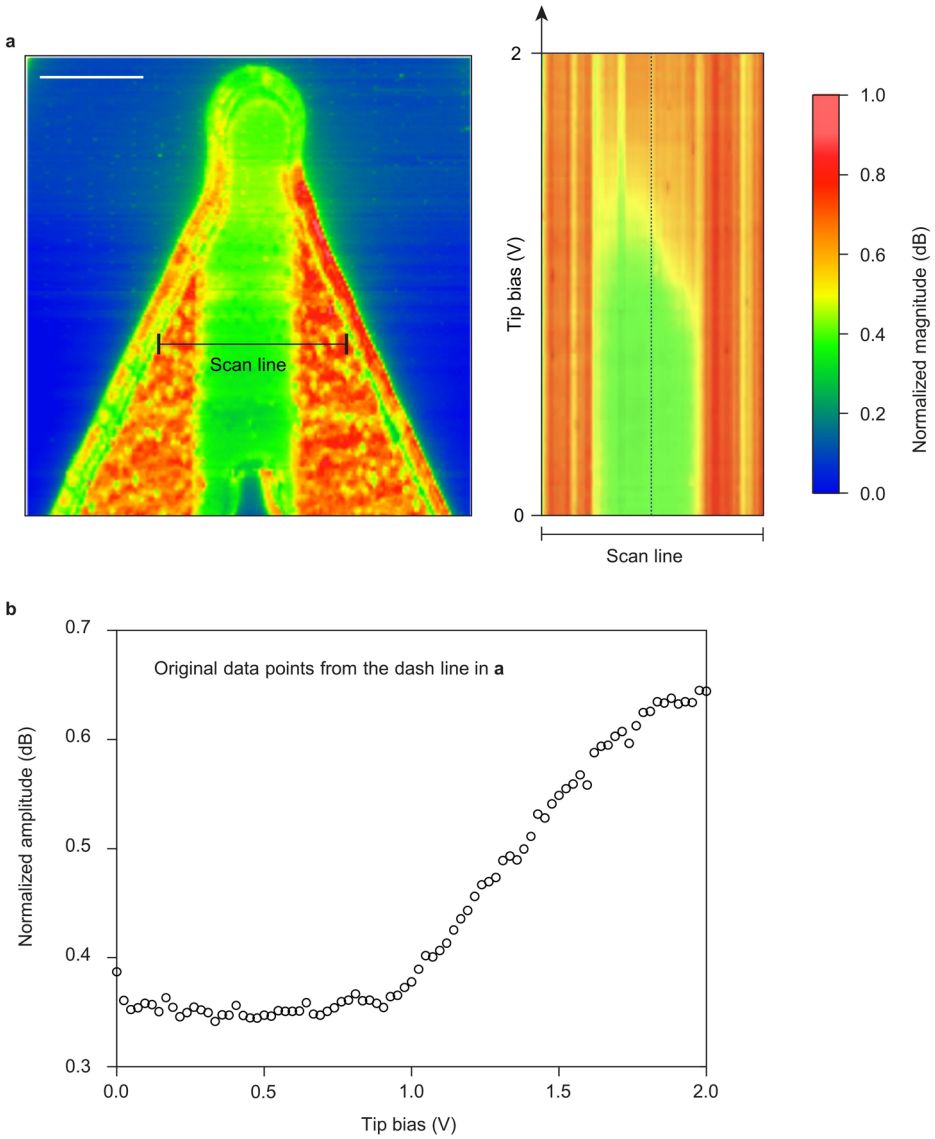

Extended Data Fig. 2 | Mapping FET's conductivity by an atomic force microscope with a bias applied by the scanning tip. a, A linear scan of the FET's conductivity was performed with a positive bias applied by the atomic force microscope. The results show a larger positive bias applied on the FET's lightly doped conduction channel yields a larger conductivity in the channel, which verifies the n-type properties of the FET's channel, which corresponds to the results by electrical transport characterizations. Scale bar: 2 μm. **b**, Original data points from the conductivity linear scan showing the FET's conduction channel turns 'ON' at the 1 V tip bias. The 'threshold voltage' didn't appear in the water-gate characterization because we used a much smaller gate bias range for scanning the water-gate characterization. Additionally, we expect the FET device is 'ON' at zero bias because the middle region is also n-type with lots of free electrons. The discrepancy between the two measurements is from their different characterization mechanisms, including the gate capacitance, method of applying the gate bias, and the information that can be read from the signals.

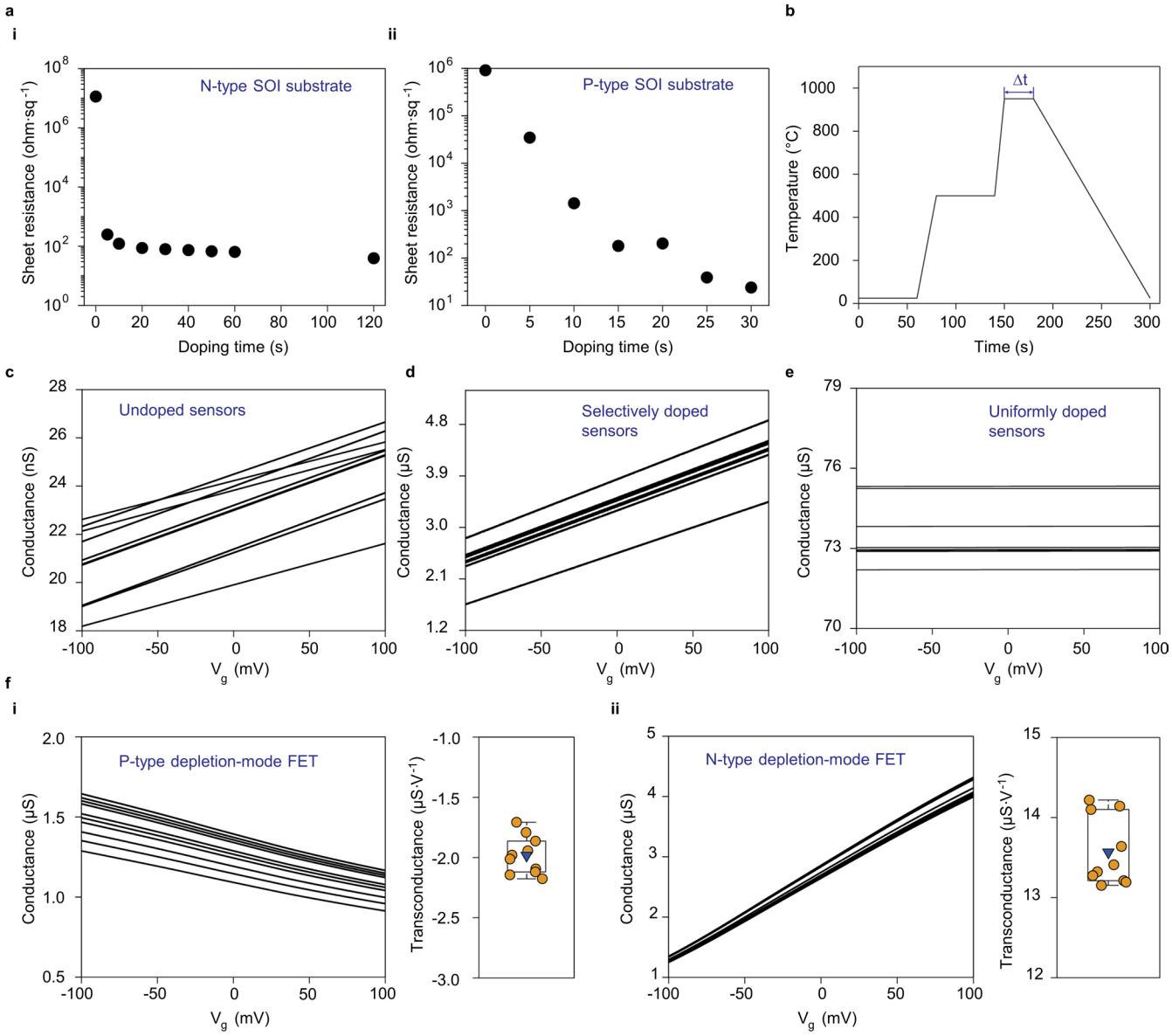

Extended Data Fig. 3 | Optimizing the FETs' electrical properties by tuning doping concentrations. a, Sheet resistances of (i) antimony doped SOI (N-type) and (ii) boron doped SOI (P-type) wafers, determined by high-temperature doping with phosphorus dopant (P509) at 950 °C for various doping times (Δt), which is defined as the period that the apex temperature was held during annealing. **b**, A typical temperature profile for driving the phosphorus dopants into the SOI wafer. The most effective doping period was at the highest temperature (950 °C), as indicated by Δt. A longer Δt generates a smaller sheet resistance of the SOI. We applied a two-step doping process: the first light doping was for the whole SOI that determined the FET's conduction channel's doping concentration; and the second heavy doping was for the whole SOI except the conduction channels. The resultant FET had an N^+NN^+ structure and worked under a depletion mode. **c-e**, Transfer characteristics of devices by various doping conditions, including (**c**) undoped, (**d**) selectively doped, and (**e**) heavily uniformly doped sensors. **f**, Transfer characteristics of (**i**) p-type and (**ii**) n-type depletion-mode FETs, showing that the n-type FETs demonstrate about six times larger transconductances (that is, sensitivities) than those p-type FETs. Therefore, we chose n-type depletion-mode FETs in this work.

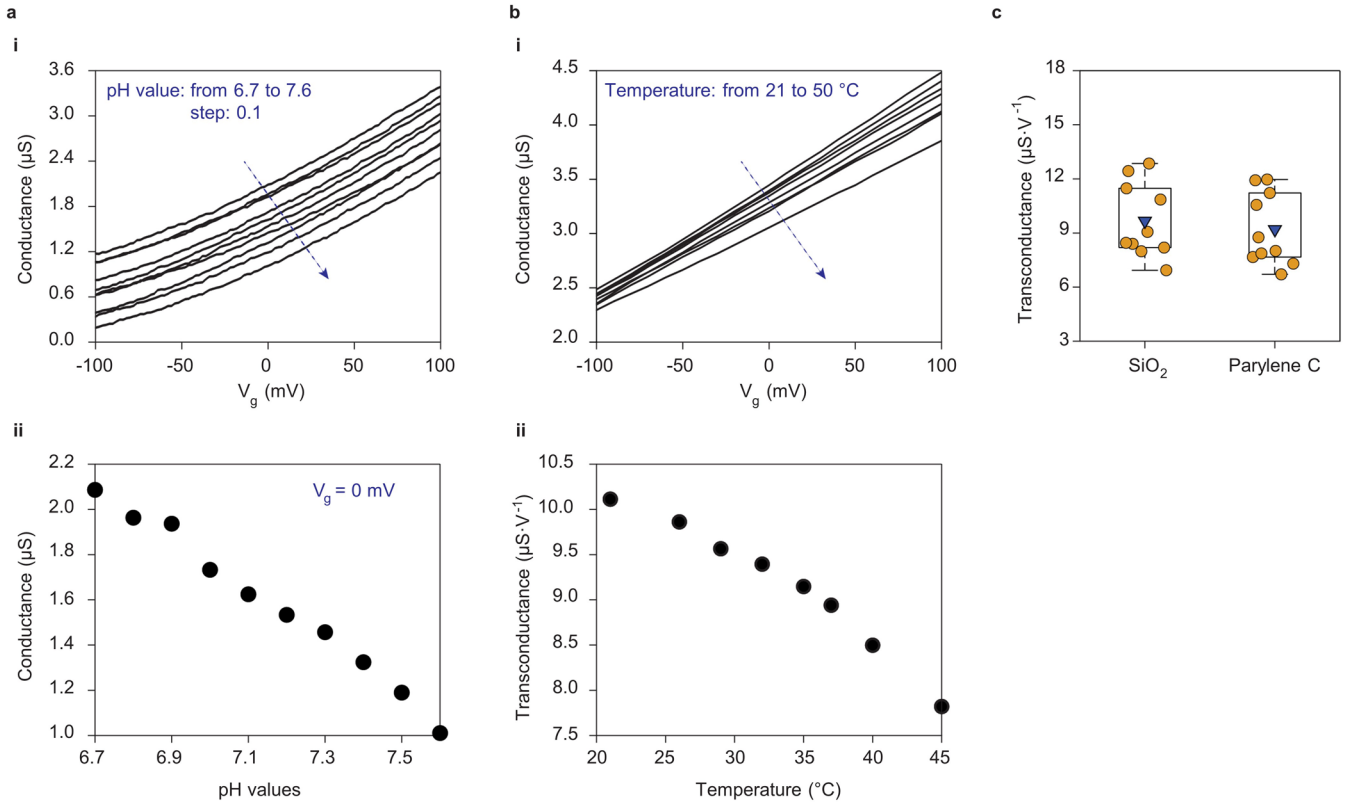

Extended Data Fig. 4 | FETs' reliability tests under various conditions. a, i, An FET's conductance with different pH of the gate solution. The transfer characteristics show high similarities, proving high reliability of the FET under various pH. The common pH for cell culturing is 7.4. **ii**, Extracted data points at zero gate bias, showing the conductance decreases with increasing the pH, giving another evidence of the n-type conductivity of the FET. **b, i**, An FET's transfer characteristics under different temperatures of the gate solution, showing the FET has excellent thermal stability and reliability under various temperatures. The common temperature for cell culturing is 37 °C. **ii**, Calculated transconductances showing the FET's transconductance decreases with increasing the temperature, which is due to the effectively reduced mobility of the charge carriers in the conduction channel. **c**, Parylene C was used as an additional gate dielectric material on top of the SiO_2 in the FET, considering SiO_2 might be soluble in biological fluids, such as extracellular solutions of cardiac muscle cells. The FETs' transconductance (that is, sensitivity) barely changed after coating the Parylene C.

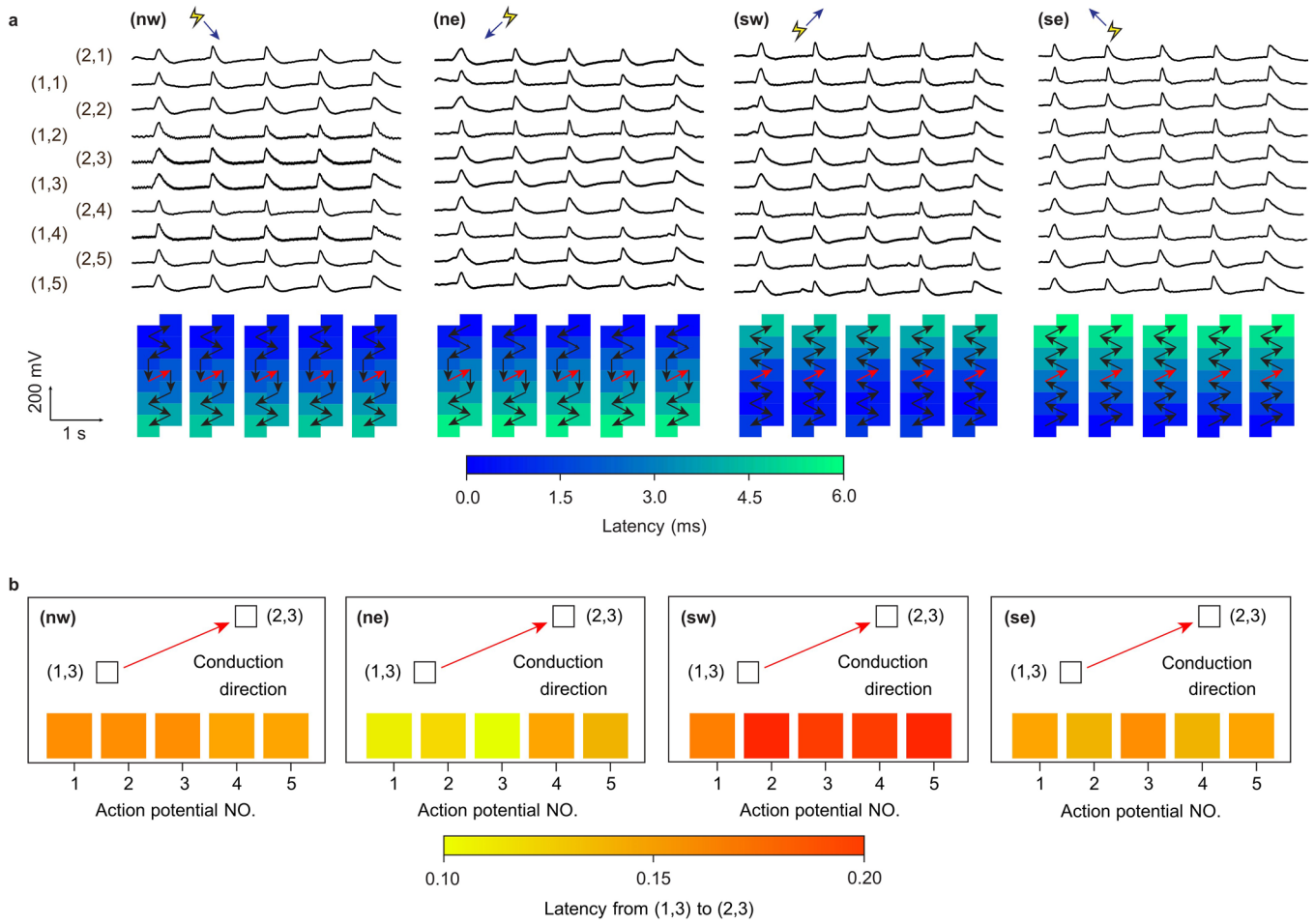

Extended Data Fig. 5 | Recordings of HL-1 cells' action potentials by a 10-FET array under electrical stimulation. a, Changing the stimulation electrode orientation from northwest (**nw**) to northeast (**ne**), southwest (**sw**), and southeast (**se**) will shift the directions of intercellular signal conductions. The first signal appeared in the FET that is relatively closer to the stimulation electrode and propagated among the cells per their coupling states, as indicated by the black arrows. The intercellular signal conduction velocity under electrical stimulation is from 35.1 to 39.3 $\mu m \cdot ms^{-1}$. The variations in the velocity are caused by the fluctuations of temperature, pH value, and ion concentration in the cell culture medium. In all scenarios, the directions of intracellular signal conductions, as indicated by the red arrows, are always the same, that is, from (1,3) to (2,3). **b**, Schematics showing the latencies of intracellular signal conductions from (1,3) to (2,3).

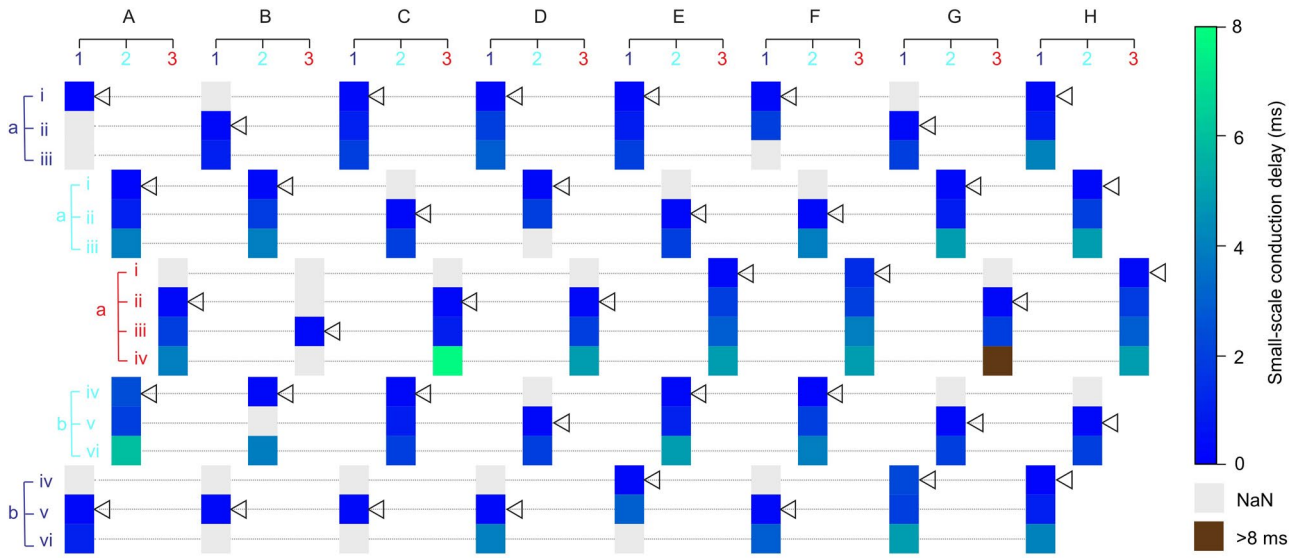

Extended Data Fig. 6 | Small-scale signal conduction within the cardiac tissue by the 128-FET array. The 128-FET array is classified into 40 units, where each arm has five units. Each unit is labelled by the combination of the located arm name (for example, 'A'), the loop number (for example, '1'), and the relative location (for example, 'a'). In each unit, the FETs are labelled in i, ii, iii, and iv. Within each unit, intercellular signal conductions via gap junctions in neighboring cells are analyzed, and the latencies are denoted in the heatmaps. The signal conduction velocity inside each unit can be calculated. For instance, in E2b, the signal transmits 70 μm from E2iv to E2vi in 5 ms. By analyzing all signal conductions within each unit, we calculated the small-scale conduction velocity (Supplementary Table 5), whose average and standard deviation are 18.8 ± 7.5 μm·ms^{-1}, which are consistent with previously reported values. The triangle for each unit indicates the selected FET that has the earliest spike within that unit. We use the selected FET in each unit as the reference point to calculate the signal conduction velocities among different units. NaN: Not a number, meaning no cellular signal was recorded.

nature portfolio

Corresponding author(s): Sheng Xu

Last updated by author(s): Aug 10, 2021

Reporting Summary

Nature Portfolio wishes to improve the reproducibility of the work that we publish. This form provides structure for consistency and transparency in reporting. For further information on Nature Portfolio policies, see our Editorial Policies and the Editorial Policy Checklist.

Statistics

For all statistical analyses, confirm that the following items are present in the figure legend, table legend, main text, or Methods section.

n/a	Confirmed	
☐	☒	The exact sample size (*n*) for each experimental group/condition, given as a discrete number and unit of measurement
☐	☒	A statement on whether measurements were taken from distinct samples or whether the same sample was measured repeatedly
☒	☐	The statistical test(s) used AND whether they are one- or two-sided *Only common tests should be described solely by name; describe more complex techniques in the Methods section.*
☒	☐	A description of all covariates tested
☒	☐	A description of any assumptions or corrections, such as tests of normality and adjustment for multiple comparisons
☐	☒	A full description of the statistical parameters including central tendency (e.g. means) or other basic estimates (e.g. regression coefficient) AND variation (e.g. standard deviation) or associated estimates of uncertainty (e.g. confidence intervals)
☒	☐	For null hypothesis testing, the test statistic (e.g. *F*, *t*, *r*) with confidence intervals, effect sizes, degrees of freedom and *P* value noted *Give P values as exact values whenever suitable.*
☒	☐	For Bayesian analysis, information on the choice of priors and Markov chain Monte Carlo settings
☒	☐	For hierarchical and complex designs, identification of the appropriate level for tests and full reporting of outcomes
☒	☐	Estimates of effect sizes (e.g. Cohen's *d*, Pearson's *r*), indicating how they were calculated

Our web collection on statistics for biologists contains articles on many of the points above.

Software and code

Policy information about availability of computer code

Data collection	The data recorded by 10-FET device and the patch-clamp were captured via Axon pCLAMP 10.3, and processed Matlab (MathWorks, USA). The data recorded by 128-FET devices was captured via DDC264 (Texas Instruments) and a customized acquisition interface (DDC264 Evaluation v3.0.4079.16447 Firmware version: 656)
Data analysis	Matlab R2019b, Fiji (ImageJ 1.53c)

For manuscripts utilizing custom algorithms or software that are central to the research but not yet described in published literature, software must be made available to editors and reviewers. We strongly encourage code deposition in a community repository (e.g. GitHub). See the Nature Portfolio guidelines for submitting code & software for further information.

Data

Policy information about availability of data

All manuscripts must include a data availability statement. This statement should provide the following information, where applicable:

- Accession codes, unique identifiers, or web links for publicly available datasets
- A description of any restrictions on data availability
- For clinical datasets or third party data, please ensure that the statement adheres to our policy

All data supporting the findings of this study are available within the Article and its Supplementary Information.

Field-specific reporting

Please select the one below that is the best fit for your research. If you are not sure, read the appropriate sections before making your selection.

☐ Life sciences ☐ Behavioural & social sciences ☐ Ecological, evolutionary & environmental sciences

For a reference copy of the document with all sections, see nature.com/documents/nr-reporting-summary-flat.pdf

Life sciences study design

All studies must disclose on these points even when the disclosure is negative.

Sample size	*Describe how sample size was determined, detailing any statistical methods used to predetermine sample size OR if no sample-size calculation was performed, describe how sample sizes were chosen and provide a rationale for why these sample sizes are sufficient.*
Data exclusions	*Describe any data exclusions. If no data were excluded from the analyses, state so OR if data were excluded, describe the exclusions and the rationale behind them, indicating whether exclusion criteria were pre-established.*
Replication	*Describe the measures taken to verify the reproducibility of the experimental findings. If all attempts at replication were successful, confirm this OR if there are any findings that were not replicated or cannot be reproduced, note this and describe why.*
Randomization	*Describe how samples/organisms/participants were allocated into experimental groups. If allocation was not random, describe how covariates were controlled OR if this is not relevant to your study, explain why.*
Blinding	*Describe whether the investigators were blinded to group allocation during data collection and/or analysis. If blinding was not possible, describe why OR explain why blinding was not relevant to your study.*

Behavioural & social sciences study design

All studies must disclose on these points even when the disclosure is negative.

Study description	*Briefly describe the study type including whether data are quantitative, qualitative, or mixed-methods (e.g. qualitative cross-sectional, quantitative experimental, mixed-methods case study).*
Research sample	*State the research sample (e.g. Harvard university undergraduates, villagers in rural India) and provide relevant demographic information (e.g. age, sex) and indicate whether the sample is representative. Provide a rationale for the study sample chosen. For studies involving existing datasets, please describe the dataset and source.*
Sampling strategy	*Describe the sampling procedure (e.g. random, snowball, stratified, convenience). Describe the statistical methods that were used to predetermine sample size OR if no sample-size calculation was performed, describe how sample sizes were chosen and provide a rationale for why these sample sizes are sufficient. For qualitative data, please indicate whether data saturation was considered, and what criteria were used to decide that no further sampling was needed.*
Data collection	*Provide details about the data collection procedure, including the instruments or devices used to record the data (e.g. pen and paper, computer, eye tracker, video or audio equipment) whether anyone was present besides the participant(s) and the researcher, and whether the researcher was blind to experimental condition and/or the study hypothesis during data collection.*
Timing	*Indicate the start and stop dates of data collection. If there is a gap between collection periods, state the dates for each sample cohort.*
Data exclusions	*If no data were excluded from the analyses, state so OR if data were excluded, provide the exact number of exclusions and the rationale behind them, indicating whether exclusion criteria were pre-established.*
Non-participation	*State how many participants dropped out/declined participation and the reason(s) given OR provide response rate OR state that no participants dropped out/declined participation.*
Randomization	*If participants were not allocated into experimental groups, state so OR describe how participants were allocated to groups, and if allocation was not random, describe how covariates were controlled.*

Ecological, evolutionary & environmental sciences study design

All studies must disclose on these points even when the disclosure is negative.

Study description	*Briefly describe the study. For quantitative data include treatment factors and interactions, design structure (e.g. factorial, nested, hierarchical), nature and number of experimental units and replicates.*
Research sample	*Describe the research sample (e.g. a group of tagged Passer domesticus, all Stenocereus thurberi within Organ Pipe Cactus National*

Research sample	*Monument), and provide a rationale for the sample choice. When relevant, describe the organism taxa, source, sex, age range and any manipulations. State what population the sample is meant to represent when applicable. For studies involving existing datasets, describe the data and its source.*
Sampling strategy	*Note the sampling procedure. Describe the statistical methods that were used to predetermine sample size OR if no sample-size calculation was performed, describe how sample sizes were chosen and provide a rationale for why these sample sizes are sufficient.*
Data collection	*Describe the data collection procedure, including who recorded the data and how.*
Timing and spatial scale	*Indicate the start and stop dates of data collection, noting the frequency and periodicity of sampling and providing a rationale for these choices. If there is a gap between collection periods, state the dates for each sample cohort. Specify the spatial scale from which the data are taken*
Data exclusions	*If no data were excluded from the analyses, state so OR if data were excluded, describe the exclusions and the rationale behind them, indicating whether exclusion criteria were pre-established.*
Reproducibility	*Describe the measures taken to verify the reproducibility of experimental findings. For each experiment, note whether any attempts to repeat the experiment failed OR state that all attempts to repeat the experiment were successful.*
Randomization	*Describe how samples/organisms/participants were allocated into groups. If allocation was not random, describe how covariates were controlled. If this is not relevant to your study, explain why.*
Blinding	*Describe the extent of blinding used during data acquisition and analysis. If blinding was not possible, describe why OR explain why blinding was not relevant to your study.*

Did the study involve field work? ☐ Yes ☐ No

Field work, collection and transport

Field conditions	*Describe the study conditions for field work, providing relevant parameters (e.g. temperature, rainfall).*
Location	*State the location of the sampling or experiment, providing relevant parameters (e.g. latitude and longitude, elevation, water depth).*
Access & import/export	*Describe the efforts you have made to access habitats and to collect and import/export your samples in a responsible manner and in compliance with local, national and international laws, noting any permits that were obtained (give the name of the issuing authority, the date of issue, and any identifying information).*
Disturbance	*Describe any disturbance caused by the study and how it was minimized.*

Reporting for specific materials, systems and methods

We require information from authors about some types of materials, experimental systems and methods used in many studies. Here, indicate whether each material, system or method listed is relevant to your study. If you are not sure if a list item applies to your research, read the appropriate section before selecting a response.

Materials & experimental systems

n/a	Involved in the study
☒	☐ Antibodies
☐	☒ Eukaryotic cell lines
☒	☐ Palaeontology and archaeology
☒	☐ Animals and other organisms
☒	☐ Human research participants
☒	☐ Clinical data
☒	☐ Dual use research of concern

Methods

n/a	Involved in the study
☒	☐ ChIP-seq
☒	☐ Flow cytometry
☒	☐ MRI-based neuroimaging

Eukaryotic cell lines

Policy information about cell lines

Cell line source(s)	Sigma Aldrich SCC065 and Dr. Xiaochen Jiang lab in Tufts University
Authentication	none of the cell line used were authenticated
Mycoplasma contamination	the cell lines were not tested for mycoplasma contamination
Commonly misidentified lines (See ICLAC register)	*Name any commonly misidentified cell lines used in the study and provide a rationale for their use.*